NEUTRINO OSCILLATIONS

Luigi Di Lella
CERN, Geneva, Switzerland

Abstract

These lectures review the status of neutrino oscillations. After an introduction to the theory of neutrino oscillation in vacuum and a survey of negative searches using man-made neutrino sources, the status of the solar neutrino problem is reviewed and explanations of the observed deficit and spectral distortions in terms of matter-enhanced oscillations are described. Expectations for ν_μ - ν_τ oscillations are then discussed and present experiments on this subject are reviewed. Recent results from the study of neutrinos produced in the Earth atmosphere and from the LSND and KARMEN are then described. Finally, future experiments are reviewed.

1. THEORY OF NEUTRINO OSCILLATIONS IN VACUUM

Neutrino oscillations are a consequence of the hypothesis of neutrino mixing first proposed by Pontecorvo [1] and independently by Maki et al.[2]. According to this hypothesis the three known neutrino flavours, ν_e, ν_μ and ν_τ, are not mass eigenstates but quantum-mechanical superpositions of three mass eigenstates, ν_1, ν_2 and ν_3, with mass eigenvalues m_1, m_2 and m_3, respectively :

$$\nu_\alpha = \sum_i U_{\alpha i} \nu_i \qquad (1)$$

In Eq. (1) $\alpha = e, \mu, \tau$ is the flavour index, $i = 1, 2, 3$ is the index of the mass eigenstates and U is a unitary 3 x 3 matrix. The relation

$$\nu_i = \sum_\alpha V_{i\alpha} \nu_\alpha \qquad (2)$$

also holds, where $V = U^{-1}$ and $V_{i\alpha} = U^*_{\alpha i}$ because U is unitary.

From Eq. (1) it follows that the time evolution of a neutrino with momentum $\vec{p}$ produced in the state ν_α at time $t = 0$ is given by

$$\nu(t) = e^{i\vec{p}\cdot\vec{r}} \sum_i U_{\alpha i} e^{-iE_i t} \nu_i \qquad (3)$$

where $E_i = \sqrt{p^2 + m_i^2}$. If the masses m_i are not all equal, the three terms of the sum in Eq. (3) get out of phase and the state $\nu(t)$ acquires components ν_β with $\beta \neq \alpha$.

The case of two-neutrino mixing is a particularly useful example. In this case the mixing matrix U is described by only one real parameter θ (the mixing angle), and Eqs. (1), (2) and (3) become, respectively

$$\nu_\alpha = \cos\theta \, \nu_1 + \sin\theta \, \nu_2$$
$$(4)$$
$$\nu_\beta = -\sin\theta \, \nu_1 + \cos\theta \, \nu_2$$

$$\nu_1 = \cos\theta \, \nu_\alpha - \sin\theta \, \nu_\beta$$
$$(5)$$
$$\nu_2 = \sin\theta \, \nu_\alpha + \cos\theta \, \nu_\beta$$

$$\nu(t) = e^{i\vec{p}\cdot\vec{r}}\left(\cos\theta e^{-iE_1 t}\nu_1 + \sin\theta e^{-iE_2 t}\nu_2\right) \tag{6}$$

where $\nu(0) = \nu_\alpha$ in Eq. (6).

The probability to detect a neutrino state ν_β at time t can then be easily calculated to be

$$P_{\alpha\beta}(t) = |\langle\nu_\beta|\nu(t)\rangle|^2 = \sin^2 2\theta \, \sin^2\left(\frac{m_2^2 - m_1^2}{4p}t\right) \tag{7}$$

where we have used the approximation, valid for $m \ll p$,

$$E_i = \sqrt{p^2 + m_i^2} \approx p\left(1 + \frac{m_i^2}{2p}\right) \tag{8}$$

It can be easily demonstrated that, for $\nu(0) = \nu_\beta$, $P_{\beta\alpha}(t)$ is also given by Eq. (7). Furthermore, we have

$$P_{\alpha\alpha}(t) = 1 - P_{\alpha\beta}(t) \tag{9}$$

Eq. (7) is expressed in natural units. In more familiar units we can write

$$P_{\alpha\beta}(L) = \sin^2 2\theta \sin^2\left(1.267\frac{\Delta m^2}{E}L\right) \tag{10}$$

where $L = ct$ is the distance from the source in metres, $\Delta m^2 = \left|m_2^2 - m_1^2\right|$ is measured in eV^2 and $E \approx p$ is the neutrino energy in MeV (the same equation holds if L is measured in km and E in GeV).

Eq. (10) describes an oscillation with amplitude equal to $\sin^2 2\theta$ and oscillation length λ given by

$$\lambda = 2.48\,\frac{E}{\Delta m^2} \tag{11}$$

where λ is expressed in metres (km) , E in MeV (GeV) and Δm^2 in eV^2. We note that, if the oscillation length λ is much shorter than the size of the neutrino source or of the detector (or of both), the periodic term in Eq. (10) averages to 1/2 and the oscillation probability becomes independent of L :

$$P_{\alpha\beta} = \frac{1}{2}\sin^2 2\theta \tag{12}$$

2. OSCILLATION EXPERIMENTS

Experiments searching for neutrino oscillations can be subdivided into two categories :

2.1 Disappearance experiments

In these experiments the flux of a given neutrino flavour is measured at a certain distance L from the source. The presence of neutrino oscillations has the effect of reducing the flux with respect to the value expected in the absence of oscillations . The probability measured by these experiments is

$$P_{\alpha\alpha}(L) = 1 - \sum_{\beta \neq \alpha} P_{\alpha\beta}(L) \tag{13}$$

The sensitivity of these experiments is limited by the systematic uncertainty on the knowledge of the neutrino flux from the source. To reduce this uncertainty a second detector close to the source is often used in order to measure directly the neutrino flux.

Disappearance experiments have been performed at nuclear reactors [3] and at accelerators [4]. The core of a nuclear reactor is an intense source of $\bar{\nu}_e$ with an average energy of ~3 MeV, which can be detected by observing the reaction $\bar{\nu}_e + p \rightarrow e^+ + n$. If a $\bar{\nu}_e$ turns into a $\bar{\nu}_\mu$ or a $\bar{\nu}_\tau$ it becomes invisible because μ^+ or τ^+ production is energetically forbidden.

Proton accelerators produce ν_μ's with energies between ~30 MeV and ~200 GeV. In disappearance experiments the ν_μ flux is measured by detecting the reaction ν_μ + nucleon $\rightarrow \mu^-$ + hadrons. The energy threshold for the reaction $\nu_\mu + n \rightarrow \mu^- + p$ on a neutron at rest is 110.2 MeV.

2.2   Appearance experiments

These experiments use beams containing predominantly one neutrino flavour and search for neutrinos of different flavour at a certain distance from the source.

The sensitivity of these experiments is often limited by the systematic uncertainty on the knowledge of the beam contamination by other neutrino flavours at the source. For example, in a typical ν_μ beam from a high-energy accelerator the ν_e contamination at the source is of the order of 1%.

Searches for ν_e and ν_τ appearance in a beam containing predominantly ν_μ have been performed at accelerators [5-6]. In these experiments the presence of ν_e's (ν_τ) in the beam is detected by observing the reaction ν_e (ν_τ) + nucleon $\rightarrow e^-$ (τ^-) + hadrons.

2.3   Review of previous experiments

So far, searches for neutrino oscillations at nuclear reactors or at proton accelerators have failed to observe any oscillation signal, with the possible exception of a recent experiment which will be described in Section 6. These negative results provide upper limits for the oscillation probability which can be converted into excluded regions in the oscillation parameter plane ($\sin^2 2\theta$, Δm^2) using Eq. (10).

Fig. 1 shows the boundaries of the exclusion regions obtained in $\bar{\nu}_e$ disappearance experiments at nuclear reactors [3]. The results from ν_e appearance experiments in a ν_μ beam [5] are shown in Fig. 2, while Fig. 3 displays the exclusion regions obtained in ν_μ disappearance experiments at accelerators using a close and a far detector [4] and the exclusion region from a ν_μ - ν_τ appearance experiment [6]. In all these figures the excluded region is on the right of the corresponding curve. At high values of Δm^2 the upper limit on the oscillation probability can be converted directly into an upper limit on the oscillation parameter $\sin^2 2\theta$ using Eq. (12).
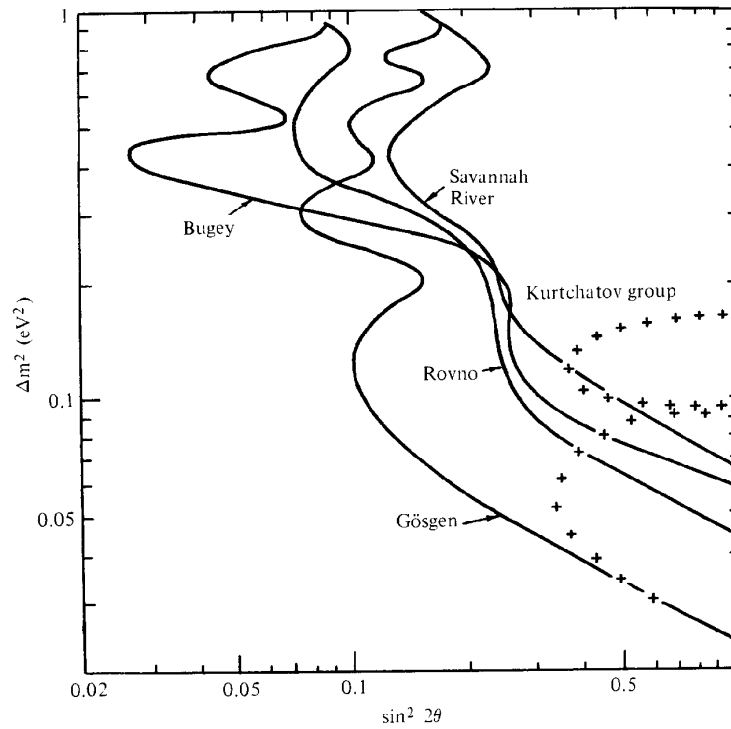

Fig. 1   Regions of the oscillation parameter plane excluded
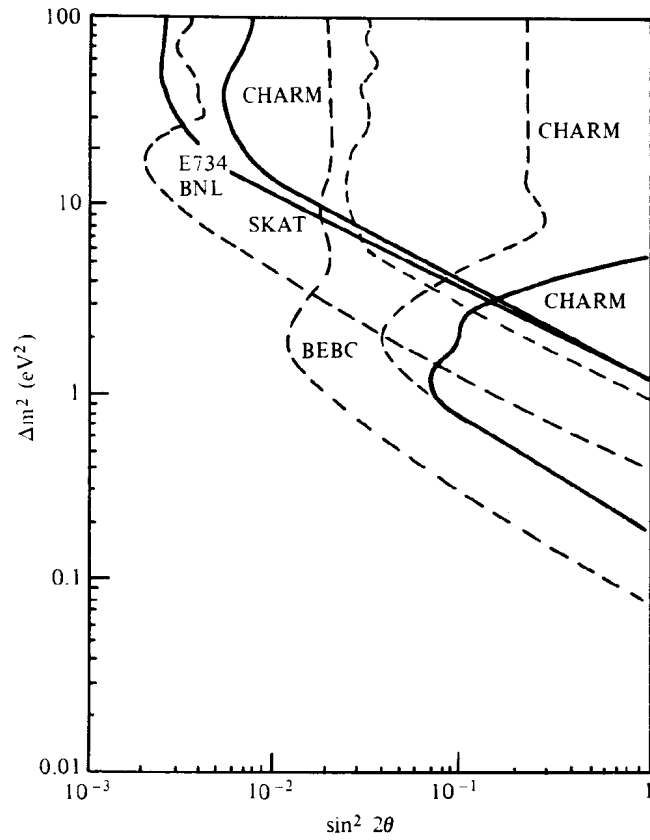by $\bar{\nu}_e$ disappearance experiments at nuclear reactors.

Fig. 2 Exclusion regions in the oscillation parameter plane from
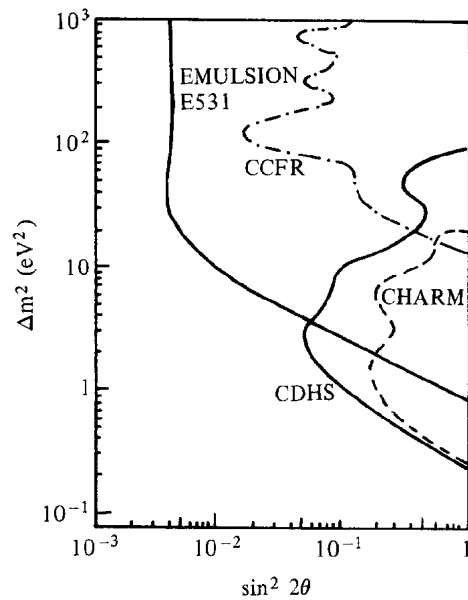v_e appearance experiments using v_μ beams.

Fig. 3 Exclusion regions in the oscillation parameter plane from v_μ disappearance
experiments (CCFR, CDHS, CHARM) and from a search for v_τ appearance
experiments using a v_μ beam (EMULSION E531).

3.   SOLAR NEUTRINOS

3.1   The Standard Solar Model

As all visible stars, the Sun was formed from the gravitational collapse of a cloud of gas consisting mostly of hydrogen and helium. This collapse produced an increase of the core density and temperature resulting in the ignition of nuclear fusion reactions. A state of hydrostatic equilibrium was reached when the kinetic and radiation pressure balanced the gravitational forces preventing any further collapse.

There are several nuclear fusion reactions occurring in the Sun core, all having the effect of transforming four protons into a He^4 nucleus :

$$4p \rightarrow He^4 + 2e^+ + 2\nu_e \tag{14}$$

This reaction is followed by the annihilation of the two positrons with two electrons, so the average energy produced by reaction (14) and emitted by the Sun in the form of electromagnetic radiation is

$$Q = (4m_p - M_{He} + 2m_e)\, c^2 - <E(2\nu_e)> \approx 26.1 \text{ MeV} \tag{15}$$

where m_p, M_{He}, m_e are the proton, He^4 nucleus and electron mass, respectively, and $<E(2\nu_e)> \approx 0.59$ MeV is the average energy carried by the two neutrinos. The Sun luminosity is measured to be [7]

$$L_o = 3.846 \text{ x } 10^{26} \text{ W} = 2.400 \text{ x} 10^{39} \text{ MeV/s} \tag{16}$$

From Eqs. (15) and (16) it is possible to calculate the rate of ν_e emission from the Sun :

$$dN (\nu_e)/dt = 2 L_o/Q \approx 1.8 \times 10^{38} \text{ s}^{-1} \qquad (17)$$

from which one can calculate the solar neutrino flux on Earth using the average distance between the Sun and the Earth (1.496×10^{11}m) :

$$\Phi_\nu \approx 6.4 \times 10^{10} \text{ cm}^{-2} \text{ s}^{-1} \qquad (18)$$

The Standard Solar Model (SSM), which has been developed and continuously updated by J. N. Bahcall during the past 20 years [8], predicts the energy spectrum of the solar neutrinos. The main assumptions of the SSM are :

 (i)   hydrostatic equilibrium;
(ii)   energy production by fusion;
(iii) thermal equilibrium (i.e., the thermal energy production rate is equal to the luminosity);
(iv) the energy transport inside the Sun is dominated by radiation.

Table I shows a list of Sun parameters.

TABLE I

Sun parameters

Luminosity	3.846×10^{26} W
Radius	6.96×10^5 Km
Mass	1.989×10^{30} Kg
Core temperature T_c	15.6×10^6 °K
Surface temperature T_s	5773 °K
Hydrogen content in the core (by mass)	34.1%
Helium content in the core (by mass)	63.9%

The age of the Sun (4.6×10^9 years) is also known. The SSM calculations are performed by adjusting the initial parameters, by evolving them to the present day and by comparing the predicted and measured properties of the Sun. The initial composition of the Sun is taken to be equal to the present day measurement of the surface abundances. If the predicted properties disagree with the measured ones, the calculations are repeated with different initial parameters until agreement is found. These calculations require the knowledge of the absolute cross-sections for nuclear reactions in a very low energy region where little information is directly available from laboratory experiments. Another important ingredient in these calculations is the knowledge of the opacity versus radius which controls the energy transport inside the Sun and the internal temperature distribution.

There are two main nuclear reaction cycles in the Sun core :

(i) The pp cycle, responsible for 98.5% of the Sun luminosity. This cycle involves the following reactions :

$$p + p \rightarrow e^+ + \nu_e + d \qquad (19a)$$

$$p + d \rightarrow \gamma + He^3 \qquad (19b)$$

$$He^3 + He^3 \rightarrow He^4 + p + p \qquad (19c)$$

where the second He^3 nucleus in the initial state of reaction (19c) is produced by another sequence of reactions (19a) and (19b).

Reactions (19a) through (19c) represent 85% of the pp cycle. In the remaining 15% reaction (19c) is replaced by the following dominant sequence of reactions :

$$He^3 + He^4 \rightarrow \gamma + Be^7 \qquad (19d)$$

$$e^- + Be^7 \rightarrow \nu_e + Li^7 \qquad (19e)$$

$$p + Li^7 \rightarrow He^4 + He^4 \tag{19f}$$

In approximately 1.9×10^{-3} of the cases reactions (19e) and (19f) are replaced by

$$p + Be^7 \rightarrow \gamma + B^8 \tag{19g}$$

$$B^8 \rightarrow Be^8 + e^+ + \nu_e \tag{19h}$$

$$Be^8 \rightarrow He^4 + He^4 \tag{19i}$$

Reaction (19a) is replaced in 0.4% of the cases by the three-body fusion reaction

$$p + e^- + p \rightarrow d + \nu_e \tag{19j}$$

Finally, in an even smaller fraction of the cases ($\sim 2.4 \times 10^{-5}$), reaction (19c) is replaced by

$$He^3 + p \rightarrow He^4 + e^+ + \nu_e \tag{19k}$$

It can be seen that in the pp cycle ν_e's are produced by the five reactions (19a), (19e), (19h), (19j) and (19k). These neutrinos will be denoted as ν_{pp}, ν_{Be}, ν_B, ν_{pep} and ν_{hep}, respectively. While ν_{pp}, ν_B and ν_{hep} have a continuous energy spectrum, ν_{Be} and ν_{pep} are mono-energetic because they are produced in two-body final states.

(ii) The CNO cycle, which involves heavier elements. This cycle consists of the following chains of reactions :

$$p + N^{15} \rightarrow C^{12} + He^4 \tag{20a}$$

$$p + C^{12} \rightarrow \gamma + N^{13} \tag{20b}$$

$$N^{13} \rightarrow e^+ + \nu_e + C^{13} \tag{20c}$$

$$p + C^{13} \rightarrow \gamma + N^{14} \tag{20d}$$

$$p + N^{14} \rightarrow \gamma + O^{15} \tag{20e}$$

$$O^{15} \rightarrow e^+ + \nu_e + N^{15} \tag{20f}$$

and

$$p + N^{15} \rightarrow \gamma + O^{16} \tag{20g}$$

$$p + O^{16} \rightarrow \gamma + F^{17} \tag{20h}$$

$$F^{17} \rightarrow e^+ + \nu_e + O^{17} \tag{20i}$$

$$p + O^{17} \rightarrow N^{14} + He^4 \tag{20j}$$

followed by reactions (20e) and (20f). As for the pp cycle, the two chains of reactions in the CNO cycle have the overall effect of transforming four protons into a He^4 nucleus. Production of ν_e occurs in reactions (20c), (20f) and (20i). These neutrinos will be denoted as ν_N, ν_O and ν_F, respectively.

Fig. 4 shows the ν_e flux as a function of energy, as predicted by the SSM for the different reactions. The ν_{pp} flux is the dominant component. However, neutrino cross-sections increase rapidly with energy (typically as E_ν^2 for energies well above

threshold), so these neutrinos are not among the easiest ones to detect because of their low energy. Fig. 4 displays also the energy threshold for the capture reaction

$$\nu_e + (A, Z) \rightarrow e^- + (A, Z + 1) \tag{21}$$

for a variety of nuclear isotopes.
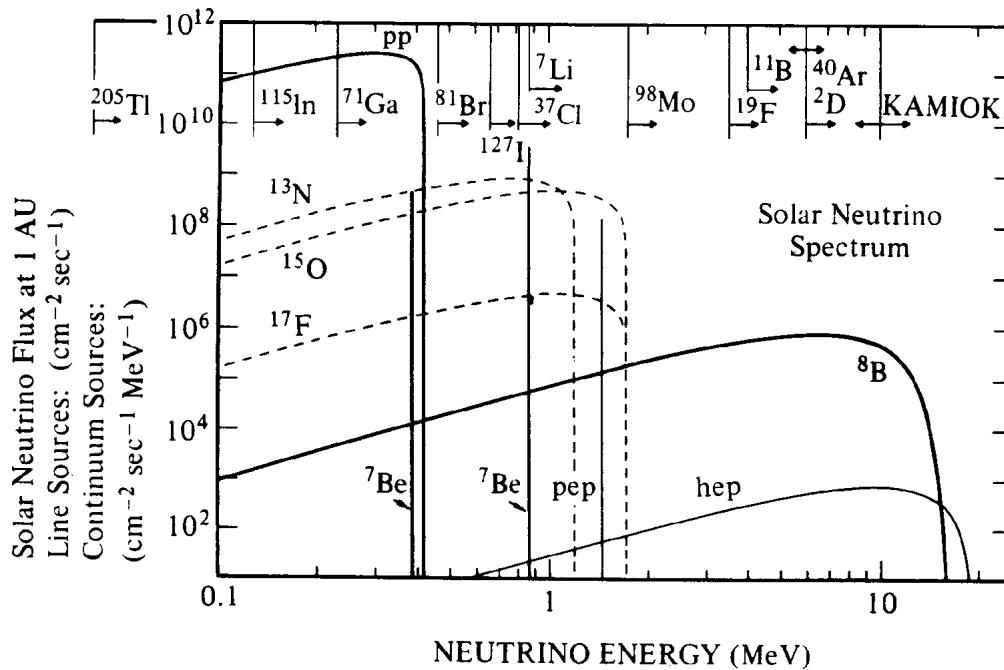
Fig. 4   Solar neutrino energy spectrum as calculated from the SSM [8].
Energy threshold for various neutrino detection processes
are shown on top.

The SSM also makes predictions on neutrino production as a function of radius, as shown in Fig. 5.

It must be finally pointed out that, while solar neutrinos arrive on Earth approximately 500 s after being produced, it takes of the order of 10^6 years for the energy produced in the same reactions to be transported from the Sun core to its surface. Thus the Sun luminosity which is measured at present is associated with neutrinos which reached the Earth ~10^6 years ago. This is not considered to be a

problem for the SSM because the Sun is a star on the main sequence, with no appreciable change of properties over $\sim 10^8$ years.
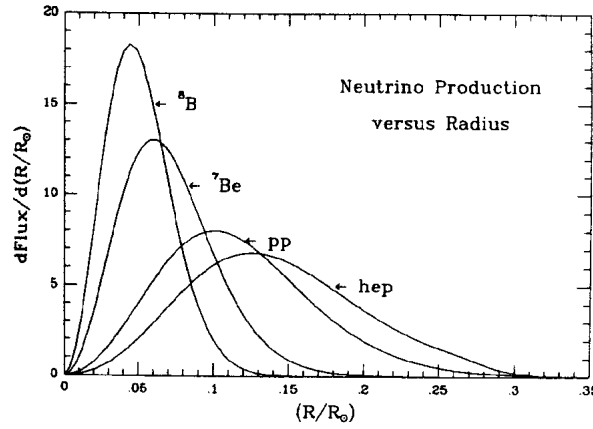
Fig. 5 Neutrino production versus distance from Sun centre,
as calculated from the SSM [8].

3.2   The Homestake experiment

Solar neutrinos were successfully detected for the first time in an experiment performed by Davis and collaborators [9] in the Homestake gold mine (South Dakota, U. S. A.). The method consists in measuring the production rate of A^{37} from the capture reaction

$$\nu_e + Cl^{37} \rightarrow e^- + A^{37} \tag{22}$$

which occurs in a 390 m^2 tank filled with 615 tonnes of perchloroethylene (C_2Cl_4, a commonly used cleaning fluid). The isotope Cl^{37} represents 24% of all natural chlorine, so there are approximately 125 tonnes of Cl^{37} in the tank. The neutrino energy threshold for reaction (22) is 0.814 MeV, so this reaction is not sensitive to the ν_{pp} component (see Fig. 4).

The tank is installed deep underground in order to reduce A^{37} production by cosmic rays. Every few months, Argon is extracted from the tank by N_2 flow. It is then separated, purified, mixed with natural Argon and used to fill a proportional

counter. The presence of A^{37} in the counter is then detected by observing its decay which occurs by electron capture with a half-life time $\tau_{1/2} = 34d$:

$$e^- + A^{37} \rightarrow \nu_e + Cl^{37} \tag{23}$$

In this reaction an X-ray or an Auger electron emitted from the atomic transition to the orbital state left empty after electron capture is detected in the proportional counter. Fig. 6 shows the counting rate in the counter as a function of time after extraction. The expected component from A^{37} decay is clearly visible, superimposed to a time-independent background. The extraction efficiency is measured by injecting a known amount of A^{37} in the tank.
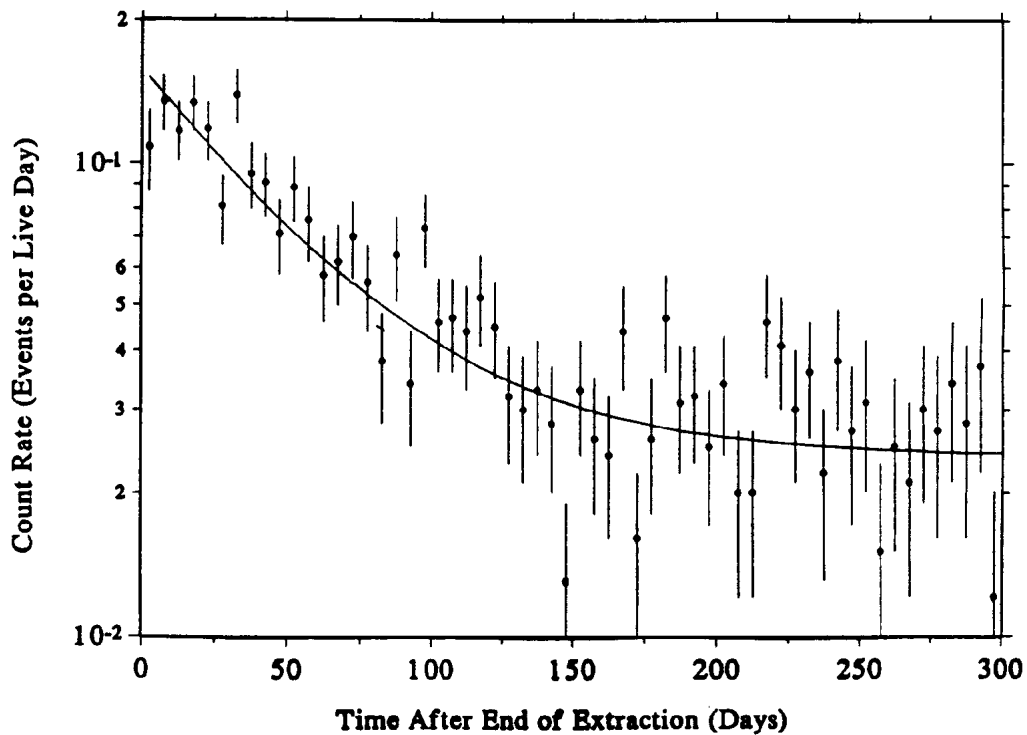
Fig. 6 Counting rate in the Homestake proportional counter as a function
of time after extraction.

Fig. 7 shows the daily A^{37} production rate, as measured over approximately 20 years. On average, this rate is of the order of 0.5 A^{37} atoms/day which illustrates the difficulty of the experiment.
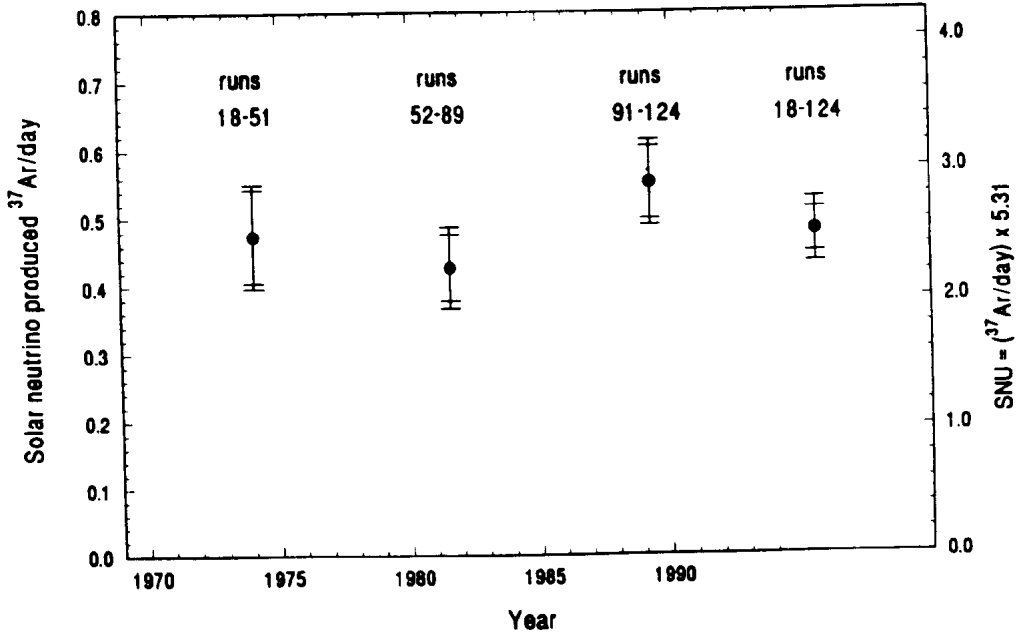
Fig. 7 Averaged daily A^{37} production rate in the Homestake experiment.

It has become customary to express the solar neutrino capture rate in Solar Neutrino Units or SNU (1 SNU corresponds to 1 capture/s from 10^{36} nuclei). The weighted average of the Homestake experiment is

$$R_{exp} (Cl^{37}) = 2.55 \pm 0.17 \pm 0.18 \text{ SNU} \qquad (24)$$

where the first error is statistical and the second one represents the systematic uncertainties.

Table 2 shows the SSM predictions, as calculated by Bahcall et al. [10].

The total rate for reaction (22) is predicted to be $R_{th} (Cl^{37}) = 8.0 \pm 3.0$ SNU, which disagrees with the measured value. An independent SSM calculation by Turck-Chièze et al. [11] predicts $R_{th} (Cl^{37}) = 6.4 \pm 1.4$ SNU which is again larger than the measured value. The ratio of the measured value to the lower theoretical prediction is

$$R_{exp} (Cl^{37}) / R_{th} (Cl^{37}) = 0.40 \pm 0.04 \pm 0.09 \qquad (25)$$

where the first error is experimental and the second one represents the theoretical uncertainty. Eq.(25) illustrates the so-called solar neutrino problem.

TABLE 2

Solar neutrino contributions to reaction (22), as predicted by the SSM [10].

Solar neutrino component	A^{37} production rate (SNU)
ν_B	6.2
ν_{Be}	1.2
ν_O	0.3
ν_{pep}	0.2
ν_N	0.1
Total	8.0 ± 3.0

3.3   The KAMIOKANDE experiment

KAMIOKANDE is a real-time experiment which uses an underground detector installed in the Kamioka mine 350 km west of Tokyo [12]. The inner detector (see Fig. 8) consists of a cylindrical tank with a diameter of 15.6 m and a height of 11.2 m, filled with 2140 tonnes of water. Approximately 20% of the tank surface are covered by 940 photomultipliers with a diameter of 50 cm and pointing towards the liquid.

The inner detector is surrounded by an additional layer of water seen by 123 photomultipliers and used to reject charged particles entering the detector from outside.

The inner detector is used as an imaging Čerenkov counter. Charged particles with $v/c \approx 1$ produce Čerenkov light at an angle of ~41° to their direction of flight and the pattern of hit photomultipliers and their relative timing provide information on the particle direction and origin in the detector volume.
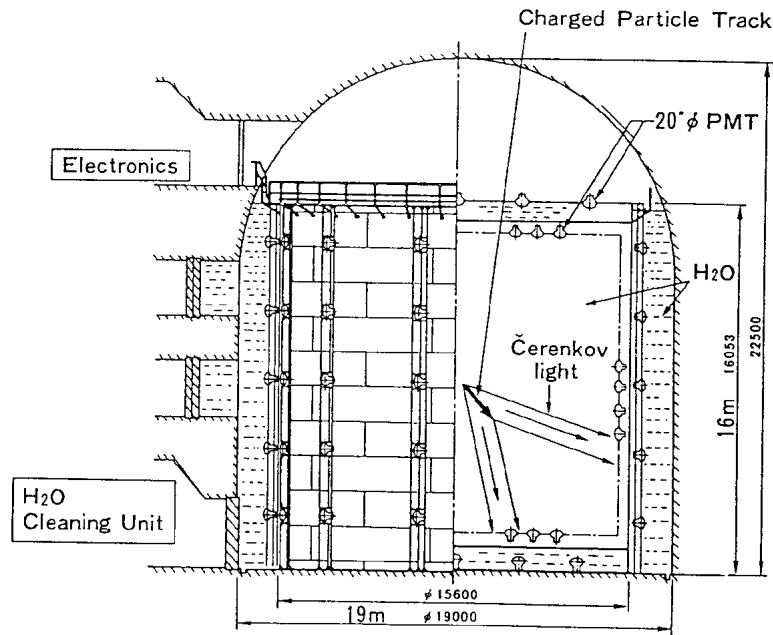
Fig. 8 The KAMIOKANDE detector.

Solar neutrinos are detected by the scattering reaction

$$\nu_e + e^- \rightarrow \nu_e + e^- \tag{26}$$

which is suppressed by approximately one order of magnitude for ν_μ and ν_τ. The detection energy threshold is set by the requirement that at least 20 photomultipliers give a signal corresponding to at least one photo-electron. This requirement corresponds to a ν_e energy of 7.5 MeV and thus the experiment is sensitive mainly to the ν_B component. Only events contained in a fiducial region of 680 tonnes in the centre of the detector are accepted.

The detected electron from reaction (26) has a very strong directional correlation with the incident neutrino. This property is used to demonstrate the solar origin of the events, as shown in Fig. 9 which displays the distribution of the angle between the electron direction and the Sun-to-Earth direction at the time of the event. The peak at 1 is due to solar neutrinos.
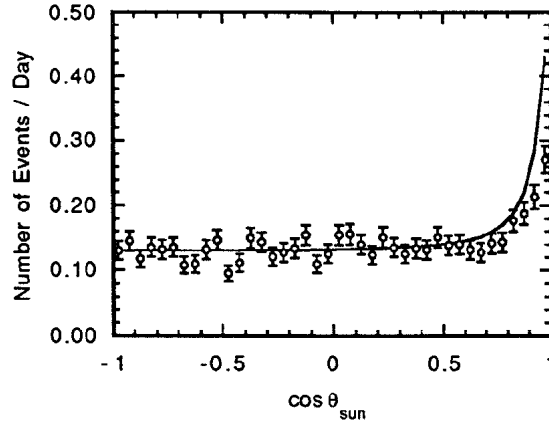
Fig. 9 Distribution of the cosine of the angle between the electron direction and the Sun-to-Earth direction, as measured in KAMIOKANDE. The curve is the prediction of the SSM, superimposed to the measured isotropic background.

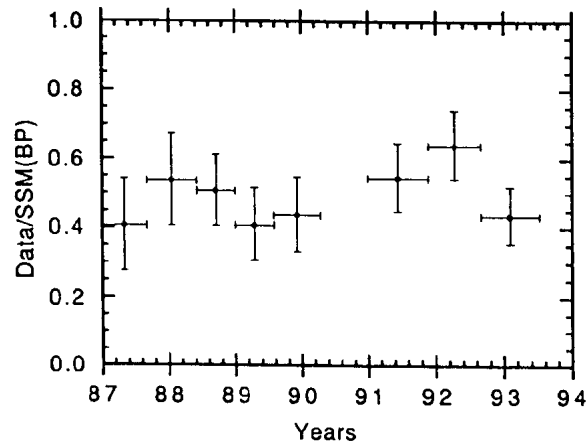KAMIOKANDE has taken data for a total of 1667 days between 1987 and 1994 (see Fig. 10).

Fig. 10 Ratio between the neutrino flux, as measured by KAMIOKANDE [12], and the SSM predictions by Bahcall et al. [10].

The neutrino flux, averaged over the entire period, is measured to be

$$\Phi_{exp} = \left(2.9 \, ^{+0.22}_{-0.21} \pm 0.35\right) \times 10^6 \, cm^{-2} s^{-1} \tag{27}$$

where the first error is statistical and the second represents the systematic uncertainties. This result is significantly lower than the SSM predictions, $\Phi_{th} = (5.7 \pm 0.7) \text{x} 10^6 \text{cm}^{-2} \text{s}^{-1}$ by Bahcall et al. [10], and $\Phi_{th} = (4.9 \pm 1.0) \text{x} 10^6 \text{cm}^{-2} \text{s}^{-1}$ by Turck-Chièze et al. [11]. Thus KAMIOKANDE confirms the existence of the solar neutrino problem first observed in the Homestake experiment.

3.4   Gallium experiments

Both the Homestake and KAMIOKANDE experiments are sensitive to solar neutrinos of relatively high energy. These neutrinos represent only a small fraction of the total solar neutrino flux and questions have been raised on the reliability of the SSM predictions. In particular, the rate of reactions (19d) and (19g), which are responsible for ν_{Be} and ν_B production, depends very strongly on the temperature of the Sun core, T_c, because of strong Coulomb repulsion effects. More specifically, the SSM predicts [8] that the ν_{Be} flux is proportional to T_c^8 while the ν_B flux, which implies the occurrence of both reactions (19d) and (19g), is proportional to T_c^{18}. A small change of T_c would therefore result in sizeable variations of the predicted ν_{Be} and ν_B fluxes.

On the contrary, the ν_{pp} component of the solar neutrino flux can be reliably predicted because these neutrinos originate from reactions (19a) through (19c) which are responsible for most of the Sun luminosity. A method to detect these neutrinos was proposed in 1966 by Kuzmin [13] who suggested to use the capture reaction

$$\nu_e + Ga^{71} \rightarrow Ge^{71} + e^- \tag{28}$$

which has a neutrino energy threshold of 0.233 MeV. Two experiments have recently used this reaction to detect solar neutrinos.

The GALLEX experiment [14] installed deep underground in the Gran Sasso National Laboratory ~ 150 km east of Rome, Italy, uses 30.3 tonnes of natural Gallium, containing 39.6% of Ga^{71}, in the form of a water solution of gallium chloride. Every three weeks, $GeCl_4$ (a highly volatile substance) is extracted from the

tank by means of N_2 flow and chemically converted to GeH_4 gas. This gas is then introduced into a proportional counter built from special low-radioactivity materials and carefully shielded against natural radioactivity. The presence of Ge^{71} from reaction (28) is then detected by observing its decay which occurs by electron capture with a half-life $\tau_{1/2}$ = 11.43 d:

$$e^- + Ge^{71} \rightarrow Ga^{71} + \nu_e \qquad (29)$$

Both the 10.37 KeV X-rays from K capture and the 1.17 KeV X-rays from L capture are detected in the counter by measuring both the signal amplitude and rise-time to provide additional rejection against background (X-rays are expected to result in very fast signals because the primary ionization which they produce is localized in space). The behaviour of the counting rate as a function of time after extraction (see Fig. 11) clearly shows the expected contribution from Ge^{71} decay.
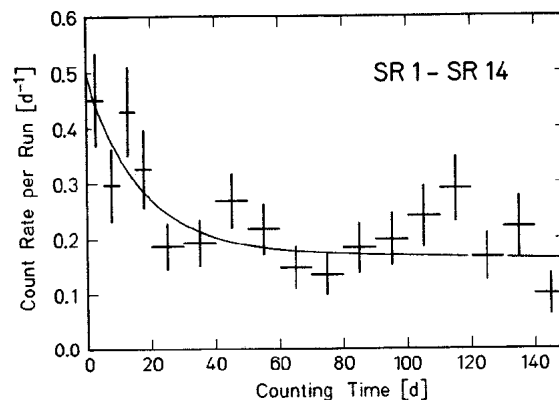
Fig. 11   Counting rate in the GALLEX proportional counter as a function of time after extraction.

The Ge^{71} extraction efficiency is measured to be 99.8% by introducing into the tank a known quantity of As^{71} which decays to Ge^{71} by electron capture.

Fig. 12 shows the solar neutrino capture rate, as measured between May 1991 and September 1993. The average value is

$$R_{exp} (Ga^{71}) = 79 \pm 10 \pm 6 \text{ SNU} \tag{30}$$

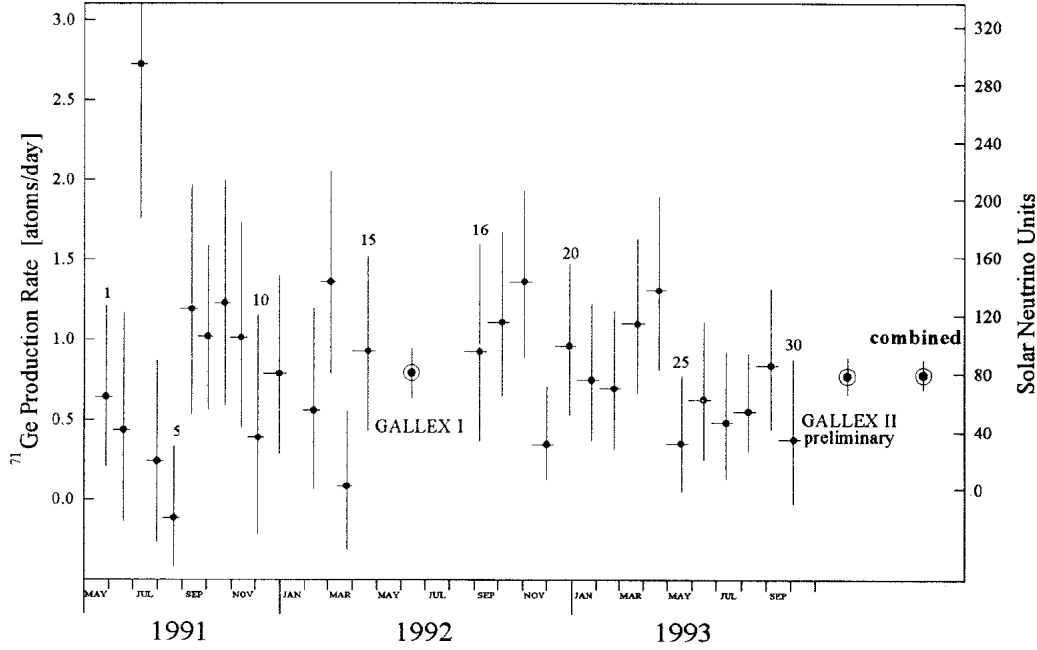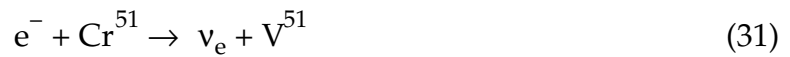where the first error is statistical and the second one represents the systematic uncertainties.

Fig. 12 Ge^{71} production rate as measured by GALLEX.

Recently, the GALLEX collaboration has performed a direct test of the neutrino detection method using artificial ν_e's from a 1.67×10^6 Curie Cr^{51} source which produces 0.750 MeV neutrinos from the decay

$$e^- + Cr^{51} \rightarrow \nu_e + V^{51} \tag{31}$$

with a half-life $\tau_{1/2} = 27.7$ d [15]. When the source is placed in the GALLEX detector, its neutrino flux is expected to increase the initial Ge^{71} production rate by a factor of ~ 15 with respect to the solar neutrino rate. The ratio between the measured and expected Ge^{71} production rate from the Cr^{51} source is measured to be 1.04 ± 0.12,

indicating that there is no significant experimental artifact or unknown errors at the 10% level which could affect the measured Ge^{71} production rate from solar neutrinos.

A second Gallium experiment, SAGE (for Soviet-American Gallium Experiment) has taken data since 1990 in the Baksan Underground Laboratory in Caucasus [16]. It uses metallic Gallium which is liquid at operating temperature, from which Ge^{71} is extracted and detected using reaction (29).

SAGE has reported results earlier than GALLEX. Fig. 13 compares the signal reported by SAGE and GALLEX as a function of time.
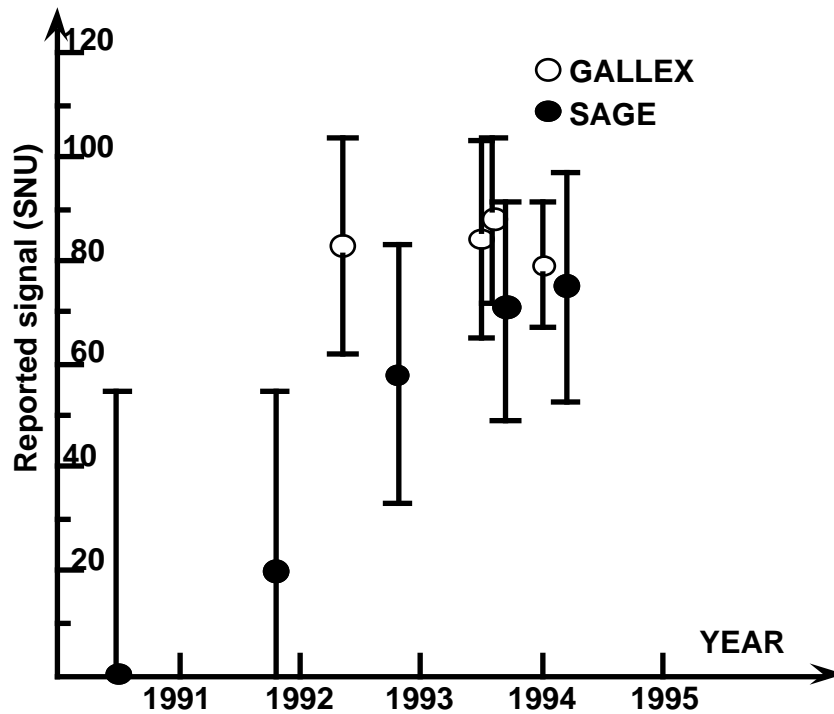
Fig. 13 Comparison between the signals reported by the GALLEX and SAGE experiments as a function of time.

After an initial preliminary result suggesting a surprisingly low solar neutrino flux, the most recent result is in good agreement with GALLEX :

$$R_{exp}\left(Ga^{71}\right) = 69 \pm 11 {}^{+5}_{-7}\text{SNU} \tag{32}$$

where the first error is statistical and the second one represents the systematic uncertainty.

Table 3 shows the SSM predictions for the Gallium experiments [10,11].

TABLE 3

Solar neutrino contributions to reaction (28), as predicted by the SSM.

Solar neutrino component	Ge^{71} production rate (SNU)	
	Ref. [10]	Ref. [11]
ν_{pp}	70.8	70.6
ν_{pep}	3.1	2.8
ν_{Be}	35.8	30.6
ν_{B}	13.8	9.3
ν_{N}	3.0	3.9
ν_{O}	4.9	6.5
Total	131.5^{+7}_{-6}	124 ± 5

As expected, the Ge^{71} production rate is dominated by the ν_{pp} contribution with sizeable contributions from ν_{Be} and ν_B and smaller contributions from ν_{pep}, ν_N and ν_O. However, for both calculations the total Ge^{71} production rate is significantly larger than the experimental values. The weighted average of the two experiments,
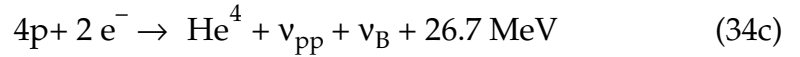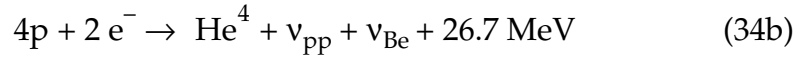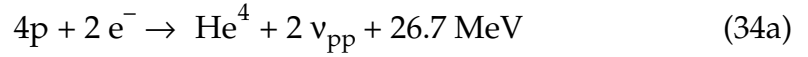
$$R_{exp} (Ga^{71}) = 74 \pm 9.5 \text{ SNU} \tag{33}$$

represents a ν_e deficit of ~ 40% with respect to the SSM predictions.

3.5 Interpretation of the solar neutrino problem

The measurement of the solar neutrino flux using three different reactions with different energy thresholds provides a way to determine directly the flux of the three dominant components from the pp cycle (ν_{pp}, ν_{Be} and ν_B), under the reasonable assumption that all other components can be neglected [17, 18, 19].

The three main reaction sequences in the p-p cycle can be rewritten in a simplified form as follows :

$$4p + 2\,e^- \rightarrow \ He^4 + 2\,\nu_{pp} + 26.7 \ MeV \tag{34a}$$

$$4p + 2\,e^- \rightarrow \ He^4 + \nu_{pp} + \nu_{Be} + 26.7 \ MeV \tag{34b}$$

$$4p + 2\,e^- \rightarrow \ He^4 + \nu_{pp} + \nu_B + 26.7 \ MeV \tag{34c}$$

Since the neutrinos emitted in these reaction sequences have different energies, the energy contributions to the Sun luminosity are different. The average neutrino energy is $<E(\nu_{pp})> = 0.265$ MeV, $E(\nu_{Be}) = 0.861$ MeV and $<E(\nu_B)> = 7.0$ MeV and the average energy release in the form of heat from reaction (34a), (34b) and (34c) is, therefore, 26.2 MeV, 25.6 MeV and 19.5 MeV, respectively.

The solar energy flux on Earth is measured to be

$$\Phi_E = 8.5 \ x \ 10^{11} \ MeV/cm^2s \tag{35}$$

Denoting by $\Phi(\nu_{pp})$, $\Phi(\nu_{Be})$ and $\Phi(\nu_B)$ the flux of ν_{pp}, ν_{Be} and ν_B on Earth, respectively, it is possible to establish a relation between Φ_E and the neutrino fluxes :

$$\Phi_E = 13.1 \ [\Phi(\nu_{pp}) - \Phi(\nu_{Be}) - \Phi(\nu_B)] + 25.6 \ \Phi(\nu_{Be}) + 19.5 \ \Phi(\nu_B) \ MeV/ \ cm^2s \tag{36}$$

On the right-hand side of Eq. (36) the first term represents the contribution from reaction (34a), because for each neutrino produced in reaction (34a) there is an energy release of 13.1 MeV and the contribution to $\Phi(\nu_{pp})$ from reactions (34b) and (34c) must be subtracted. Similarly, for each produced ν_{Be} (ν_B) there is an energy release of 25.6 (19.5) MeV which contributes to the second (third) term in Eq. (36).

As the purpose of this analysis is to study deviations from the SSM predictions, we express the neutrino fluxes as

$$\Phi(\nu_{pp}) = x_{pp}\,\Phi_{SSM}(\nu_{pp}) \tag{37a}$$

$$\Phi(\nu_{Be}) = x_{Be}\,\Phi_{SSM}(\nu_{Be}) \tag{37b}$$

$$\Phi(\nu_B) = x_B\,\Phi_{SSM}(\nu_B) \tag{37c}$$

where

$$\Phi_{SSM}(\nu_{pp}) = 6.0 \times 10^{10}\,\text{cm}^{-2}\,\text{s}^{-1} \tag{38a}$$

$$\Phi_{SSM}(\nu_{Be}) = 4.9 \times 10^{9}\,\text{cm}^{-2}\,\text{s}^{-1} \tag{38b}$$

$$\Phi_{SSM}(\nu_B) = 5.7 \times 10^{6}\,\text{cm}^{-2}\,\text{s}^{-1} \tag{38c}$$

are the SSM predictions of Bahcall et al. [10] and the parameters x_{pp}, x_{Be} and x_B describe the deviations of the measurements from these predictions.

Using Eqs. (35), (37) and (38), Eq. (36) becomes

$$1 = 0.92\,x_{pp} + 0.072\,x_{Be} + 4.2 \times 10^{-5}\,x_B \tag{39}$$

As the solar neutrino capture rate from Ga^{71} depends linearly on the neutrino fluxes, it can be expressed in terms of x_{pp}, x_{Be} and x_B with the help of Table 3 and neglecting all other contributions.

$$70.8\, x_{pp} + 35.8\, x_{Be} + 13.8\, x_B = 74 \pm 9.5 \text{ SNU} \qquad (40)$$

where the right-hand side of the equation is the combined result of the Gallium experiments (Eq. 33).

Similarly, with the help of Table 2 the Homestake result can be written as

$$1.2\, x_{Be} + 6.2\, x_B = 2.55 \pm 0.25 \text{ SNU} \qquad (41)$$

In the Kamiokande experiment the flux $\Phi(\nu_B)$ is measured directly (see Eq. 27). After combining the statistical and systematic error and dividing by $\Phi_{SSM}(\nu_B)$, as given by Eq. (38c), one obtains

$$x_B = 0.51 \pm 0.07 \qquad (42)$$

Eq. (39) can be used to express x_{pp} as a function of x_{Be} and x_B and to eliminate x_{pp} from Eq. (40) which becomes

$$30.3\, x_{Be} + 13.8\, x_B = -3.0 \pm 9.5 \text{ SNU} \qquad (43)$$

It can easily be seen that any two equations (41), (42), (43) give a solution for x_{Be} which has a negative, unphysical value, although consistent with zero within errors. The result of simultaneous fit to the three equations using x_{Be} and x_B as fitting parameters with the conditions $x_{Be} \geq 0$ is shown in Fig. 14. The best fit values are $x_{Be}=0$, $x_B=0.43$ with $\chi^2 = 2.2$. Also shown in Fig. 14 are the 1σ to 5σ contours, calculated assuming gaussian errors, together with the SSM predictions. It can be seen that the

best fit differs from the SSM predictions by at least 3σ, even if the temperature of the Sun core is allowed to vary.
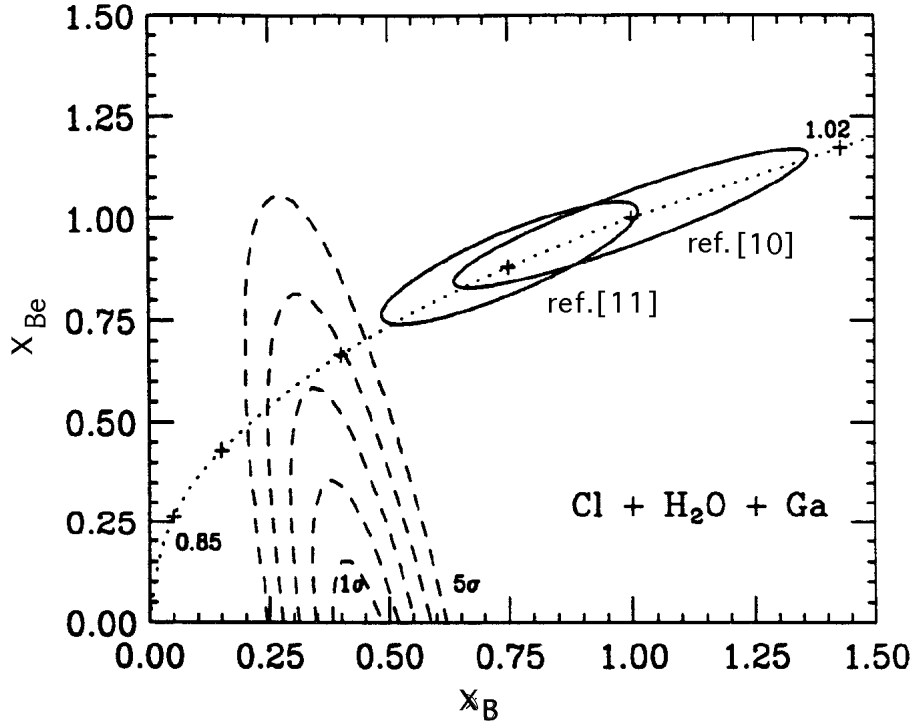

Fig. 14 Best fit to Eqs. (41), (42) and (43) and 1σ to 5σ contours (dashed curves). The solid ellipses are SSM predictions. The dotted line is the SSM expectation for variable temperature of the Sun core measured in units of the SSM prediction of Ref. [10], $T_c = 15.6 \times 10^6\ {}^\circ K$ (the crosses on this line correspond to temperature values of 0.85, 0.90, 0.95, 0.984, 1.000 and 1.02).

By using the best fit values $x_{Be}=0$, $x_B=0.43$ in Eq. (40) one obtains $x_{pp}=0.96 \pm 0.13$ which agrees with the SSM prediction for the ν_{pp} contribution to the solar neutrino flux.

The absence of ν_{Be} is intriguing because Be^7 is needed to form B^8 (reaction 19g) and neutrinos from B^8 decay (reaction 19h) have been observed in the KAMIOKANDE experiment. However, if Be^7 is produced in the Sun core, then reaction (19e), which is responsible for ν_{Be} production, occurs at a rate which is approximately three orders of

magnitude faster than reaction (19g) because the latter is strongly suppressed by Coulomb repulsion effects .

There are three possible explanations to this puzzle :

(i)   At least two of the three measurements of the solar neutrino flux are wrong;

(ii)   There is a basic flaw in the SSM, resulting in unreliable predictions of the solar neutrino flux;

(ii)   The ν_{Be}'s are produced as ν_e in the core of the Sun but are no longer ν_e when they reach the Earth.

This last explanation, which we assume to be the correct one, implies the occurrence of neutrino oscillations.

3.6   Vacuum oscillation solution to the solar neutrino problem

The range of oscillation parameters which would explain the apparent absence of ν_{Be} in the solar neutrino flux on Earth can be estimated by requiring that all ν_e's with energy E=0.861 MeV are no longer ν_e when they reach the Earth. Setting $P_{\alpha\beta}$ (L) =1 in Eq. (10), where L=1.496 $x10^{11}$m is the average distance between the Sun and the Earth, one obtains $\sin^2 2\theta = 1$ and

$$\Delta m^2 = \frac{\pi}{1.27}\left(n + \frac{1}{2}\right)\frac{E}{L} \approx 1.4x10^{-11}\left(n + \frac{1}{2}\right)eV^2 \qquad (44)$$

where n $\geq$ 0 is an integer. However, from Eq. (10) it can be easily shown that the solution n=0 produces no significant suppression of the neutrino flux above 7.5 MeV, in disagreement with the KAMIOKANDE result. Similarly, solutions with large values of n are excluded because in these cases the oscillation probability varies very rapidly with energy resulting in a reduction of the ν_e capture rate in Cl^{37} by only a factor of 2.

The result from the most recent analysis of the solar neutrino problem in terms of vacuum oscillations [20] is shown in Figure 15. Several islands of allowed

parameters are possible. However, while these solutions are all mathematically acceptable, they result from a precise numerical relation among three physical quantities (Δm^2, the distance between the Sun and the Earth and the ν_{Be} energy) which should be totally uncorrelated.
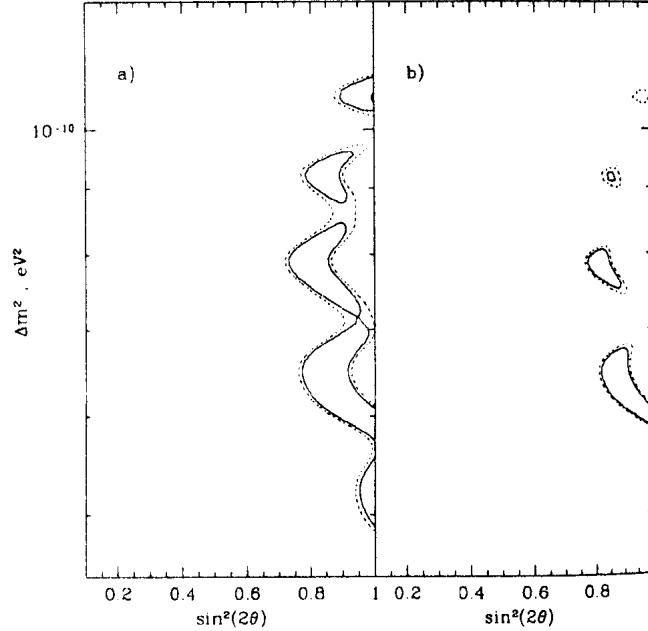

Fig. 15   Regions of the $\sin^2 2\theta$, Δm^2 plane allowed at the 90% (solid line) and 95% (dashed line)
confidence level by the solar neutrino results using the SSM predictions of Ref. [10]
including (a) or without including (b) the theoretical uncertainties.

More seriously, all of these solutions require large mixing angles. This seems rather unplausible in comparison with the parameters of the CKM matrix which describes quark mixing in the Standard Model [21]. A more plausible solution to the solar neutrino problem can be found if one takes into account the properties of neutrino propagation through the dense solar core in the presence of mixing.

3.7   Theory of neutrino oscillations in matter

It was first pointed out by Wolfenstein [22] that neutrino oscillations in dense matter differ from oscillations in vacuum if ν_e's are involved. This effect arises from coherent neutrino scattering at 0° which, in addition to the Z-boson exchange amplitude (the same for all three neutrino flavours), in the case of ν_e's has a

contribution from W-boson exchange with the matter electrons (see the relevant Feynman graphs in Fig. 16).
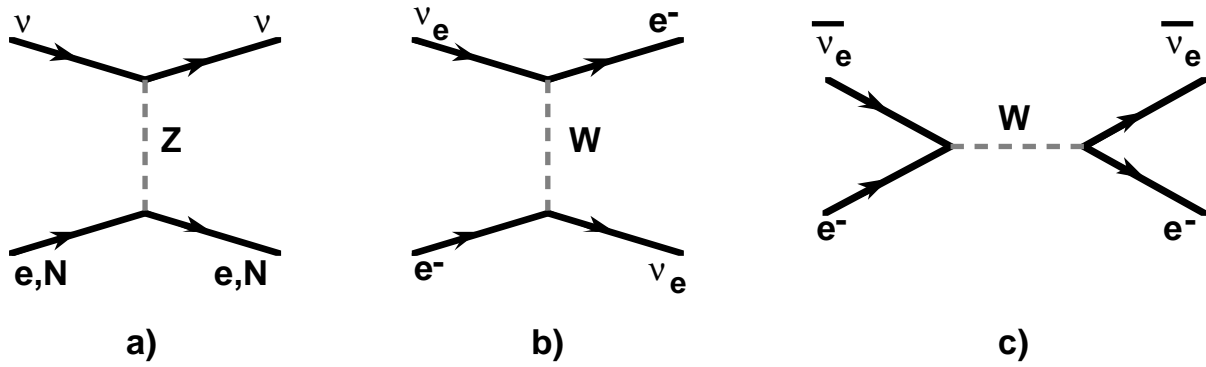

Fig. 16   Feynman graphs for neutrino scattering in matter : (a) neutrino-nucleon or neutrino-electron scattering by Z boson exchange (the same for all three neutrino types); b) ν_e-electron and (c) $\bar{\nu}_e$-electron scattering by W boson exchange.

Since scattering at 0° is a coherent process involving an extended target, the propagation of neutrinos in matter can be described by adding to the Hamiltonian a potential energy term which for the diagram of Fig. 16b is given by

$$V_W = \sqrt{2}G_F N_e \approx 7.63\text{x}10^{-14}\frac{Z}{A}\rho \text{ eV} \qquad (45)$$

where G_F is the Fermi coupling constant, N_e is the number of electrons per unit volume, ρ is the matter density in g/cm^3 and the ratio Z/A is the number of electrons per nucleon.

We consider the case of two-neutrino mixing between ν_e and ν_μ :

$$\nu_e = \nu_1 \cos \theta_v + \nu_2 \sin \theta_v \qquad (46a)$$

$$\nu_\mu = -\nu_1 \sin \theta_v + \nu_2 \cos \theta_v$$

where θ_v is the mixing angle in vacuum. We assume that $\theta_v < 45°$ and $m_2 > m_1$, where m_1 (m_2) is the ν_1 (ν_2) mass value. The evolution equation is

$$i\frac{d\Psi}{dt} = H\Psi \tag{47}$$

where

$$\Psi = \begin{pmatrix} \nu_e \\ \nu_\mu \end{pmatrix} \tag{48}$$

is a two-component vector describing the neutrino state at time t and the Hamiltonian H is a 2 x 2 matrix :

$$H = \sqrt{p^2 + M^2} + V_Z \begin{vmatrix} 1 & 0 \\ 0 & 1 \end{vmatrix} + V_W \begin{vmatrix} 1 & 0 \\ 0 & 0 \end{vmatrix} \tag{49}$$

where M^2 is the square of the mass matrix and V_Z is the potential energy term resulting from Z boson exchange. By using the approximation

$$\sqrt{p^2 + M^2} \approx p + \frac{M^2}{2p} \approx E + \frac{M^2}{2p}$$

the Hamiltonian can be rewritten as

$$H = (E + V_Z) \begin{vmatrix} 1 & 0 \\ 0 & 1 \end{vmatrix} + \frac{1}{2E} \begin{vmatrix} M^2_{ee} + 2EV_W & M^2_{e\mu} \\ M^2_{\mu e} & M^2_{\mu\mu} \end{vmatrix} \tag{50}$$

where

$$M^2_{ee} = \frac{1}{2}\left(\mu^2 - \Delta m^2 \cos 2\theta_v\right) \tag{51a}$$

$$M^2_{e\mu} = M^2_{\mu e} = \frac{1}{2}\Delta m^2 \sin 2\theta_v \tag{51b}$$

$$M^2_{\mu\mu} = \frac{1}{2}\left(\mu^2 + \Delta m^2 \cos 2\theta_v\right) \tag{51c}$$

with $\mu^2 = m_1^2 + m_2^2$ and $\Delta m^2 = m_2^2 - m_1^2$. Obviously, the first term of the Hamiltonian produces no mixing between ν_e and ν_μ.

The study of the ideal case of ν_e's produced in a medium of constant density is mathematically rather simple and is very useful to understand the physics of neutrino oscillations in matter. In this case the Hamiltonian is time-independent and the mass eigenstates can be found by diagonalising the second matrix in Eq. (50).

The two mass eigenvalues in matter are

$$m^2 = \frac{1}{2}\left(\mu^2 + \xi\right) \pm \frac{1}{2}\sqrt{(\Delta m^2 \cos 2\theta_v - \xi)^2 + (\Delta m^2)^2 \sin^2 2\theta_v} \qquad (52)$$

and the mixing angle in matter, θ_m, is given by the equation

$$\tan 2\theta_m = \frac{\Delta m^2 \sin 2\theta_v}{\Delta m^2 \cos 2\theta_v - \xi} \qquad (53)$$

where

$$\xi = 2V_w E \approx 1.526 \times 10^{-7}\,(Z/A)\rho E \;\; eV^2 \qquad (54)$$

In Eq. (54) ρ is in g/cm^3 and the neutrino energy E is in MeV.

The behaviour of the two mass eigenvalues as a function of ξ is illustrated in Fig. 17.

Eq. (53) shows that, even if θ_v is very small, for $\xi = \Delta m^2 \cos 2\theta_v$ the denominator vanishes and the mixing angle in matter, θ_m, is equal to 45°, which corresponds to maximal mixing. This resonant behaviour was first noticed by Mikheyev and Smirnov [23] some years after Wolfenstein's original formulation of the theory of neutrino oscillations in matter. At the resonant value of ξ the difference between the two eigenstates is minimal and is equal to $\Delta m^2 \sin 2\theta_v$.
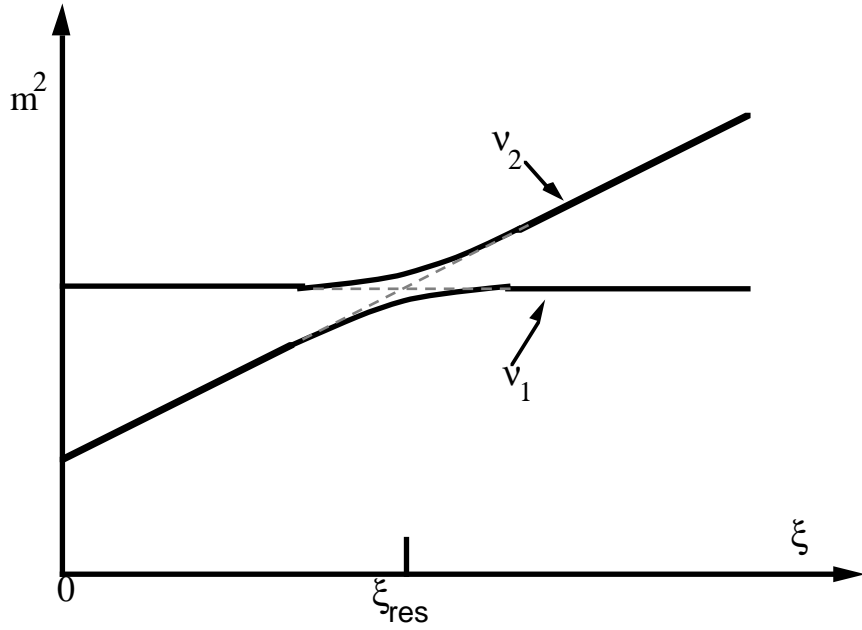
Fig. 17   Neutrino mass eigenvalues in matter as a function of ξ for the case of small mixing angle in vacuum. On the right-hand side of the resonant value, ξ_{res}, ν_2 is mostly ν_e while on the left-hand side ν_2 is mostly ν_μ.

The oscillation length in matter, λ_m, is longer than in vacuum and is given by

$$\lambda_m = \lambda_v \frac{\Delta m^2}{\sqrt{\left(\Delta m^2 \cos 2\theta_v - \xi\right)^2 + (\Delta m^2)^2 \sin^2 2\theta_v}} \tag{55}$$

where λ_v is the oscillation length in vacuum given by Eq. (11). The maximum value of λ_m is reached at resonance, where $\lambda_m = \lambda_v / \sin 2\theta_v$.

The potential energy term V_w changes sign for $\bar{\nu}_e$ (see the Feynman graph of Fig. 16c). As a consequence, the difference between the two mass eigenvalues increases monotonically with density. There is no resonance, therefore, in the case of antineutrinos.

3.8   Application to the solar neutrino problem

For neutrinos propagating through the Sun, the density ρ varies along the trajectory from a value higher than 100 g/cm^3 in the core to much less than 1 g/cm^3

in the outermost layers. The ratio Z/A also varies across the Sun because of the varying hydrogen abundance. Hence, in Eq. (47) the Hamiltonian depends on time. For a given set of mixing parameters m_1, m_2 and θ_v, Eq. (47) can be solved numerically with the initial condition

$$\Psi(0) = \begin{pmatrix} 1 \\ 0 \end{pmatrix} \tag{56}$$

which represents a pure ν_e state, using the SSM predictions for the solar density, Z/A ratio and distribution of neutrino origins inside the Sun core.

The ideal case of constant density discussed in Section 3.7 represents a good approximation to a class of solutions of relatively short oscillation length for which the variation of the solar density over an oscillation length is negligible (the so-called adiabatic solutions) :

$$\frac{1}{\rho} \frac{d\rho}{dr} \lambda_m << 1 \tag{57}$$

where r is the distance from the Sun centre. For such solutions the neutrino can be described as superposition of mass eigenstates with slowly varying eigenvalues and mixing angle. In this case, if for a ν_e at production the condition $\xi > \Delta m^2 \cos 2\theta_v$ is satisfied, then θ_m is larger than 45° (see Eq. 53) and the dominant mass eigenstate is ν_2. If, furthermore, the adiabaticity condition (57) is satisfied also at resonance, where λ_m is maximal, then the $\nu_2 \rightarrow \nu_1$ transition probability is negligible and the dominant mass eigenstate is still ν_2 when the neutrino emerges from the Sun. However, the ν_2 eigenstate in vacuum is mostly ν_μ because $\theta_v < 45°$. Thus the Mikheyev - Smirnov resonance offers an elegant way to explain the solar neutrino problem even if the mixing angle in vacuum is small.

It must be pointed out that, in the case of small mixing angle, only the ν_e's produced with $\xi > \Delta m^2 \cos 2\theta_v$ may emerge from the Sun as ν_μ's as a result of the

Mikheyev-Smirnov effect. As ξ depends linearly on the neutrino energy E (see Eq. 54), this condition is satisfied only by neutrinos produced above a critical energy which depends on the mixing parameters.

The results from the latest analysis of the solar neutrino data in terms of matter enhanced oscillations [24] are shown in Fig. 18. For each experiment the measured event rate corresponds to a region of allowed parameters in the $\sin^2 2\theta_v$, Δm^2 plane. This region consists of a vertical band at large mixing angles, of a horizontal band at constant Δm^2 corresponding to adiabatic solutions and extending to small mixing angles, and of another band merging into the two previous ones for which the allowed values of $\sin 2\theta_v$ decrease with increasing Δm^2.

Since the processes used to detect solar neutrinos have different energy thresholds, these regions do not coincide and the oscillation parameters which describe all available data are defined by their overlap. An additional region of the $\sin^2 2\theta$, Δm^2 plane defined by $\sin^2 2\theta > 0.02$ and 2×10^{-6} eV$^2 < \Delta m^2 < 10^{-5}$ eV^2 is excluded by the absence of day - night effect in KAMIOKANDE [25]. This happens because with such parameters one expects enhanced ν_μ - ν_e oscillations for neutrinos crossing the Earth, resulting in an increase of the ν_e flux at nights which is not observed experimentally.

As shown in Fig. 18, the best fit values of the oscillation parameters taking into account matter effects are

$$\sin^2 2\theta = 6.5 \times 10^{-3}; \; \Delta m^2 = 6.1 \times 10^{-6} \text{ eV}^2 \tag{58a}$$

or

$$\sin^2 2\theta = 0.62; \quad \Delta m^2 = 9.4 \times 10^{-6} \text{ eV}^2 \tag{58b}$$

One must add to these two solutions the vacuum oscillation solutions described in section 3.6 for which Δm^2 is in the range 10^{-11} - 10^{-10} eV^2 and $\sin^2 2\theta > 0.7$.

Unfortunately, there is no way to detect oscillations with such parameters in experiments using neutrinos from reactors or accelerators. Even in the more favourable case of the large Δm^2 solutions (Eqs. 58a and 58b), for $\bar{\nu}_e$ from nuclear

reactors (average energy 3 MeV) the oscillation probability is maximal at a distance of ~700 km from the source (see Eq. 11). Similarly, for a neutrino beam of 1 GeV from an accelerator the required distance between source and detector is ~ 200 000 km.

It must be finally noted that an identical explanation of the solar neutrino problem would be obtained under the assumption of ν_e - ν_τ oscillations.
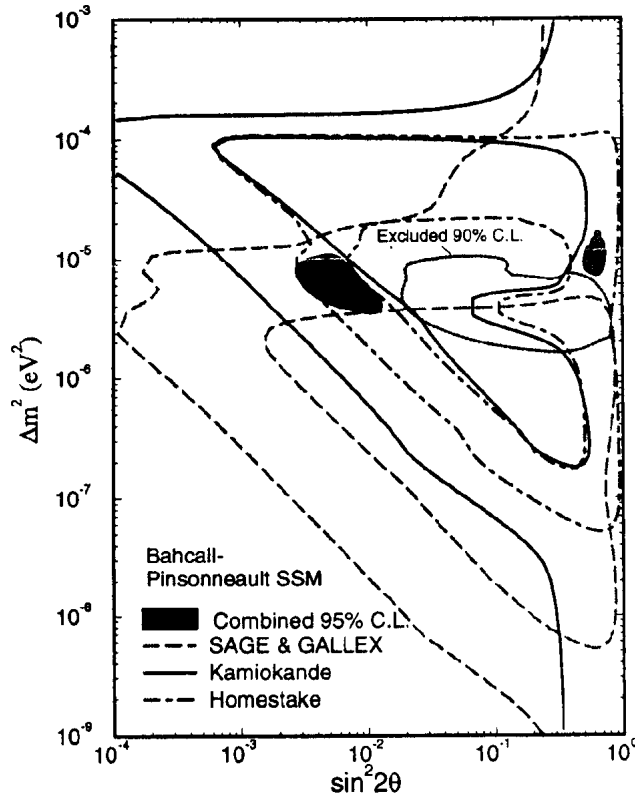

Fig. 18   The allowed regions of the Homestake, KAMIOKANDE and Gallium experiments, taking into account the Earth effect in the KAMIOKANDE experiment and using the SSM predictions of Ref. [10].

4.   SEARCH FOR ν_μ - ν_τ OSCILLATIONS

4.1   The "see-saw" model

The so-called "see-saw" model [26] is a reasonable theoretical proposal which tries to explain why neutrinos are much lighter than the charged leptons or quarks in the same fermion generation.

In this model it is conjectured that each fermion generation contains a massless Dirac neutrino field describing left-handed neutrinos, ν_L, and right-handed

antineutrinos, $\bar{\nu}_R$, and an additional field describing the two helicity states N_L and N_R of a Majorana neutrino. The mass terms in the Lagrangian are written as [27]

$$m\bar{\nu}_L N_R + \frac{1}{2} M \overline{N}_L^c N_R = \frac{1}{2}\left(\bar{\nu}_L, \overline{N}_L^c\right)\begin{pmatrix} 0 & m \\ m & M \end{pmatrix}\begin{pmatrix} \nu_R^c \\ N_R \end{pmatrix} \tag{59}$$

where m and M are parameters of the theory with $m << M$.

The eigenvalues of the square of the mass matrix in Eq. (50) give the mass values of the two physical neutrino states for each generation :

$$m_1 \approx m^2/M \qquad ; \qquad m_2 \approx M \tag{60}$$

(the heavier the second neutrino, the lighter the first one, hence the name of the model).

If, furthermore, one assumes that M has the same value for all three generations, then it is possible to obtain a relation among the masses of the three light neutrinos if one takes for m the value of the charged lepton or of the $I_3 = 1/2$ quark in each generation. In the former case

$$m(\nu_e) : m(\nu_\mu) : m(\nu_\tau) = m_e^2 : m_\mu^2 : m_\tau^2 \tag{61a}$$

while in the latter case

$$m(\nu_e) : m(\nu_\mu) : m(\nu_\tau) = m_u^2 : m_c^2 : m_t^2 \tag{61b}$$

In both cases one has $m(\nu_\mu) >> m(\nu_e)$, so that, assuming that the solar neutrino problem is the result of ν_e - ν_μ oscillation, Δm^2 is equal to $[m(\nu_\mu)]^2$ to a very good approximation. From the small mixing angle solution (Eq. 58a) one obtains

$$m(\nu_\mu) \approx 2.5 \times 10^{-3} \text{ eV} \qquad\qquad (62)$$

from which, using Eq. (61a) one has

$$m(\nu_e) \approx 6 \times 10^{-8} \text{ eV} \qquad ; \qquad m(\nu_\tau) \approx 0.7 \text{ eV} \qquad (63a)$$

Alternatively, using Eq. (61b) one obtains

$$m(\nu_e) \approx 2.5 \times 10^{-8} \text{ eV} \qquad ; \qquad m(\nu_\tau) \approx 32 \text{ eV} \qquad (63b)$$

where we have used the values $m_u = 5$ MeV, $m_c = 1.5$ GeV and $m_t = 170$ GeV.

From Eqs. (60) and (62) one further obtains $M \approx 5 \times 10^6$ TeV or 8×10^8 TeV, using Eq. (61a) or (61b), respectively. Obviously, in both cases the second physical neutrino is too heavy to be experimentally observed.

The range of values for the ν_τ mass in the see-saw model (between ~ 1 and ~ 30 eV) can be compared with the cosmological upper limit for the sum of the three neutrino masses which is of the order of 50 eV [28]. Thus, with such masses, the ν_τ could be, at least partially, an important component of the dark matter in the Universe.

More importantly, the ν_μ - ν_τ oscillation length for a neutrino beam energy of 30 GeV would be in the range from 100 m to 200 km. Such oscillations can be observed using high-energy neutrino beams from accelerators if the mixing angle is not too small.

4.2   The CERN experimental programme on neutrino oscillations.

Two experiments are presently taking data in the wide-band neutrino beam from the CERN 450 GeV SPS with the aim of detecting ν_μ - ν_τ oscillations.

The method adopted by both experiments consists in detecting τ^- production with a sensitivity corresponding to a ν_τ/ν_μ ratio of ~ 2×10^{-4}. Such a value is

approximately three orders of magnitude larger than the value expected from D_S production by the primary proton beam, followed by the decay $D \rightarrow \tau \nu_\tau$. The observation of τ^- production could only result, therefore, from ν_μ - ν_τ oscillations.

The two experiments are installed one behind the other at a distance of ~ 820 m from the proton target. A pair of pulsed magnetic lenses located after the target produces a parallel wide-band beam of positive hadrons. Neutrinos from π or K decay reach the detectors, while iron and earth shielding is used to absorb surviving hadrons and to range out decay muons. The distance between the proton target and the end of the decay tunnel is 414 m. Fig. 19 shows the expected neutrino energy spectrum.
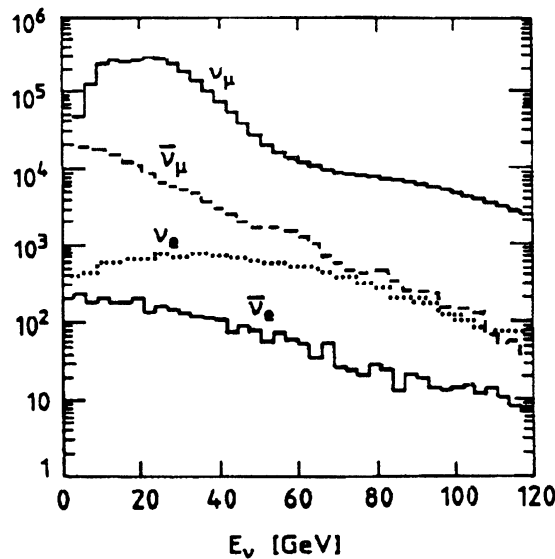

Fig. 19   Expected neutrino flux from the CERN wide-band beam. The ordinate gives the number of neutrinos per m^2 per GeV for 10^9 protons on target.

The CHORUS experiment is located just upstream of the NOMAD experiment. CHORUS (CERN Hybrid Oscillation Research apparatUS) aims at detecting the characteristic decay of the short-lived τ lepton in nuclear emulsion [29]. The apparatus is shown in Fig. 20. It consists of an emulsion target with a total mass of ~ 800 kg followed by an electronic tracking detector made of scintillating fibres, an air-core hexagonal magnet, high-resolution calorimetry and a muon spectometer. The

hexagonal magnet provides a field of 0.1 T, over a length of 0.75m, oriented along the sides of an hexagon with no radial dependence. It is used to determine the charge and momentum of low-energy particles with a resolution $\sigma(p)/p \sim 20\%$ for momenta between 2 and 10 GeV. The calorimeters consist of scintillating fibres embedded in lead and provide a resolution $\sigma(E)/E \sim 0.13/\sqrt{E}$ and $\sim 0.35/\sqrt{E}$ (E in GeV) for electromagnetic and hadronic showers, respectively.
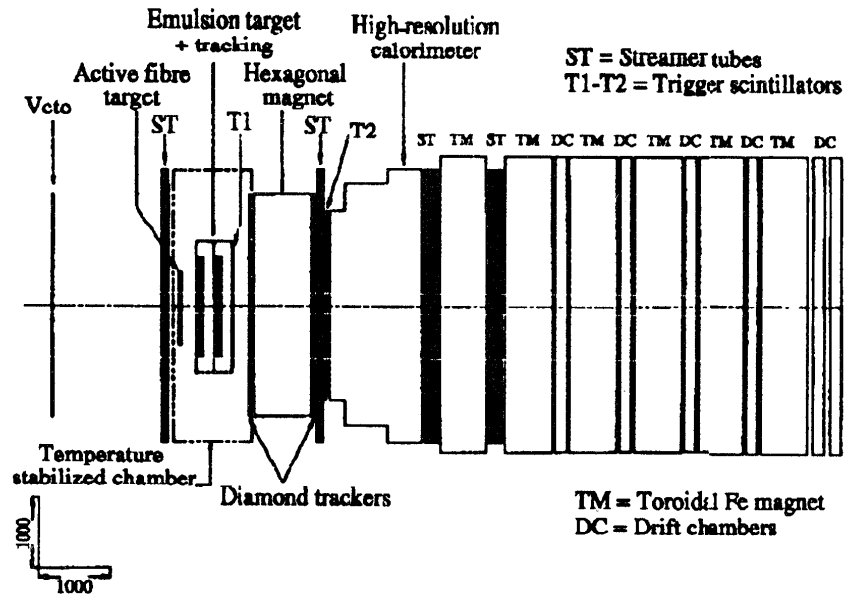

Fig. 20 Layout of the CHORUS detector.

Neutrino events with a μ^-, a negatively charged hadron or three charged hadrons with negative total charge are selected and one of the tracks is followed back to the exit point from the emulsion target for further scanning and measurement.

The large number of ν_μ charged-current (CC) or neutral-current (NC) interactions which would satisfy this first selection is reduced by more than one order of magnitude by applying kinematical criteria which distinguish these events from ν_τ CC interactions. For a total of 2.4×10^{19} protons on target, which correspond to a run of two years, one expects 5×10^5 ν_μ CC interactions in the emulsion target,

which are reduced to ~ 3 x 10^4 events to be scanned by rejecting event configurations with the muon momentum and the total momentum of all other detected particles at opposite azimuthal angles. Similarly, the expected number of 1.5 x 10^5 ν_μ NC interactions is reduced to ~ 10^4 events to be scanned by rejecting the events in which the missing transverse momentum is opposite in azimuth to the momentum of the negative hadron (or of the three charged hadrons).

The method used to follow the tracks of selected events back into the emulsion target is illustrated in Fig. 21. A special emulsion sheet which is replaced approximately every three weeks during the run is mounted between the emulsion target and the fibre tracker. With the reconstruction accuracy of the latter, the track position on this sheet is predicted within an area of 360 μm x 360μm. In this area one finds, on average, only 5 muon tracks which are rejected by angular measurement. The search is then continued in an area of 20μm x 20μm into the emulsion target, with negligible background despite the long exposure time of the target. Using a computer-assisted microscope, the time needed to follow back the track to the primary vertex is typically 15 minutes and with 20 measuring tables it is possible to analyse ~ 5 x 10^4 event/year.
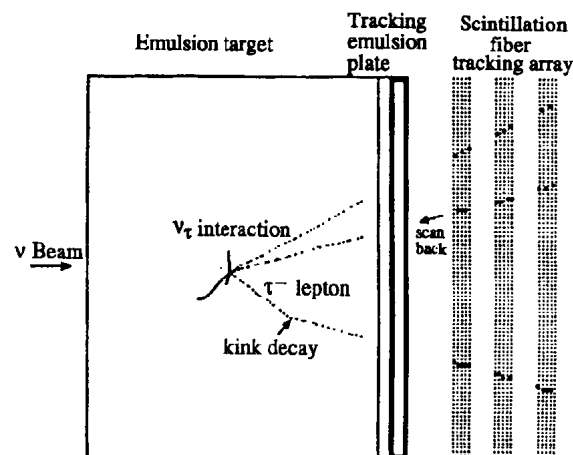

Fig. 21   Expected configuration of a typical $\nu_\tau N \rightarrow \tau^- X$ event in the emulsion and
scintillating fibre tracker. The average τ^- decay length is of the order of one
millimetre.

CHORUS started data taking in May 1994; at the end of October 1995 the emulsion target was removed and developed (a quarter of the target had already been developed and replaced at the end of 1994). Fig. 22 shows a beautiful example of a ν_μ CC event containing a charmed meson decaying to a μ^+. This event serves to illustrate the excellent space resolution which can be achieved by means of the emulsion technique.
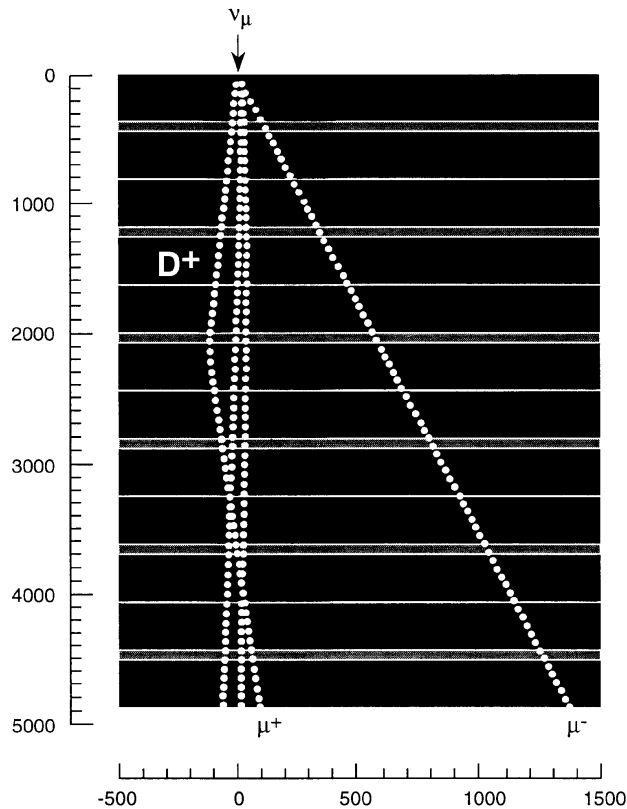

Fig. 22   A ν_μ CC event as reconstructed in the CHORUS emulsion. The event contains a
short-lived particle (most likely a D^+ meson) decaying to a μ^+. The scale of both the
abscissa and ordinate is in micrometres.

Table 4 shows the expected sensitivity of the CHORUS experiment to the three τ^- decay modes being considered, for an exposure of 2.4×10^{19} protons on target. Also listed in Table 4 is the number of events $\left(N_\tau^*\right)$ expected from ν_μ - ν_τ oscillations with $\Delta m^2 > 40 eV^2$ and $\sin^2 2\theta = 5 \times 10^{-3}$, a value corresponding to the present upper limit (see section 2 and Fig. 3). The observation of one event consistent with

background gives an upper limit of 3.5 events from ν_μ - ν_τ oscillations at the 90% confidence level, equivalent to the limit $\nu_\tau/\nu_\mu < 1.6 \times 10^{-4}$.

TABLE 4

CHORUS sensitivity to ν_τ CC interactions. The number of events corresponds

to a run of 2.4×10^{19} protons on target.

$\tau-$ decay mode	Branching ratio	Efficiency	N_τ^*	Background events
$\nu_\tau \mu^- \bar{\nu}_\mu$	0.0178	0.084	20	0.15
$\nu_\tau h^- + n\pi^\circ$	0.50	0.040	25	0.5
$\nu_\tau \pi^- \pi^- \pi^+ + n\pi^\circ$	0.14	0.055	10	0.5
Total			55	1.15

For $\Delta m^2 > 40$ eV^2 this corresponds to the limit

$$\sin^2 2\theta < 3.3 \times 10^{-4}$$

at the 90% confidence level.

An additional two-year run is scheduled for 1996-97 with a new emulsion target.

NOMAD (Neutrino Oscillation MAgnetic Detector) aims at identifying τ^- production and decay using only kinematical criteria [30]. Such a method was proposed a long time ago [31], but previous neutrino detectors never had the required resolution.

The NOMAD experiment had a later start with respect to CHORUS, both because of a later approval and because of technical problems with one of the detector components in 1994. The apparatus became fully operational in August 1995 but useful data have been recorded since May with a reduced target mass. Data taking in parallel with CHORUS is scheduled until the end of 1997.

The apparatus is shown in Fig. 23. It is based on the UA1 magnet [32] which provides a horizontal magnetic field of 0.4 T perpendicular to the beam axis over a volume of 3.6 x 3.5 x 7.0 m^3.

The main detector components are :

(i)   A system of 44 drift chambers, each with a thickness equivalent to ~ 0.02 radiation lengths (r.l.) and consisting of three wire planes for stereo reconstruction of charged particle tracks. These chambers also act as the neutrino target, providing a mass of ~ 2.5 tonnes over a fiducial area of 2.6 x 2.6 m^2. The average density of this target is 0.1g/cm^3. The momentum resolution for charged hadrons and muons is

$$\frac{\sigma(p)}{P} \approx \frac{0.05}{\sqrt{L}} \oplus \frac{0.008p}{\sqrt{L^5}}$$

where L is the track length in metres and p is the particle momentum in GeV. In this expression the first term arises from multiple scattering and the second one from measurement errors.
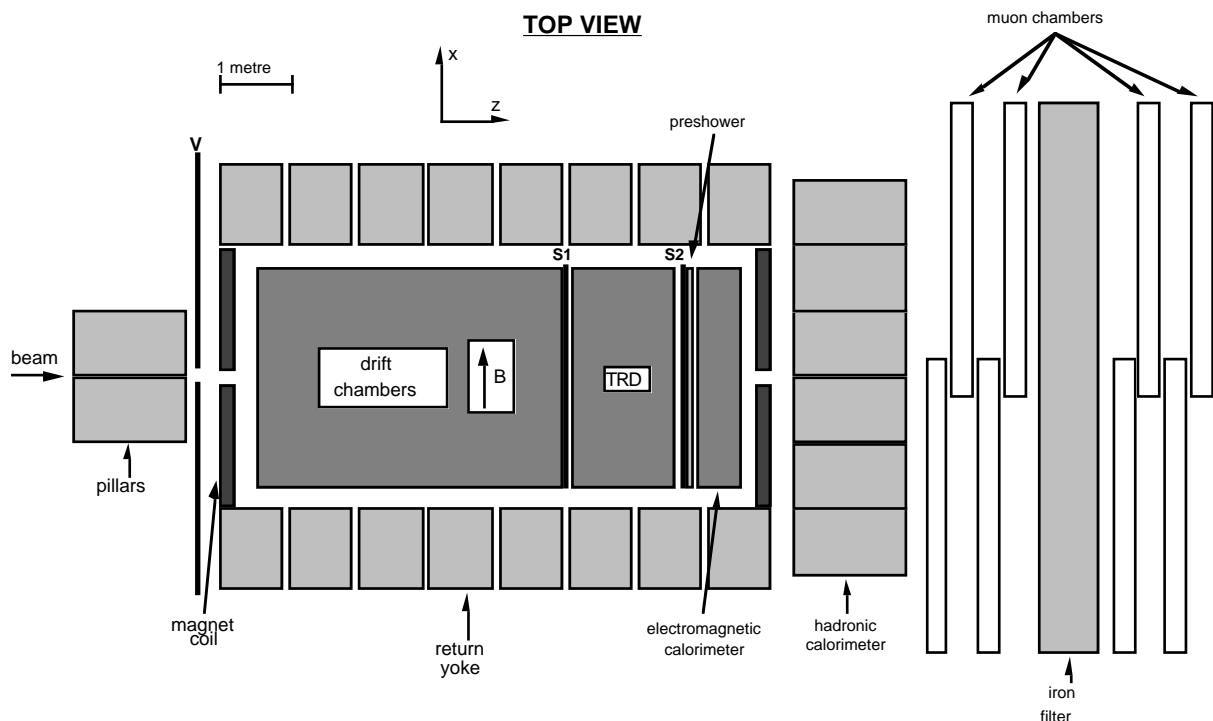

Fig. 23 Top view of the NOMAD detector.

(ii)   Nine modules of transition radiation detectors (TRD) for electron identification. Each module (see Fig. 24) consists of a radiator followed by a layer of vertical straw-tubes filled with a Xe-CH_4 mixture to detect the transition radiation X-rays produced by charged particles with $E/m > 10^3$ when they cross the radiator. Five additional drift chambers are interspersed among the TRD modules to track charged particles in this region.

(iii)   An electromagnetic calorimeter [33] consisting of 875 lead-glass counters equipped with special photo-tetrodes for operation in the magnetic field. This calorimeter is located behind a "preshower" detector consisting of two orthogonal layers of proportional tubes behind a 1.6 r.l. thick converter. The energy resolution for electrons and photons is

$$\frac{\sigma(E)}{E} \approx \frac{0.03}{\sqrt{E}} \oplus 0.01$$

where E is in GeV.

(iv)   A hadronic calorimeter made of a multi-layer iron-scintillator sandwich.

(v)   Ten large-area muon chambers [34] arranged in two stations separated by an 80 cm thick iron wall.

The NOMAD experiment aims at detecting τ^- production by observing both leptonic and hadronic decay modes of the τ^-. The decay $\tau^- \rightarrow \nu_\tau e^- \bar{\nu}_e$ is particularly attractive because the main background results from ν_e CC events which are only ~1% of the total number of neutrino interactions in the target fiducial volume. This background is rejected by considering the azimuthal separation ϕ_{eh} between the electron momentum and the total hadron momentum, and the azimuthal separation ϕ_{mh} between the latter and the missing transverse momentum (see Fig. 26a). As

shown in Figures 26b and 26c, for ν_e CC events ϕ_{eh} is peaked at 180° while the correlation is much looser in the case of $\tau^- \to \nu_\tau e^- \bar{\nu}_e$ decay. Furthermore, in a large fraction of decays τ^- decays the missing transverse momentum resulting from the two outgoing neutrinos is at opposite azimuthal angles to the total hadron momentum. Hence it is possible to define a region of the (ϕ_{mh}, ϕ_{eh}) plane which is mainly populated by τ^- decays, with very little background from ν_e CC events.
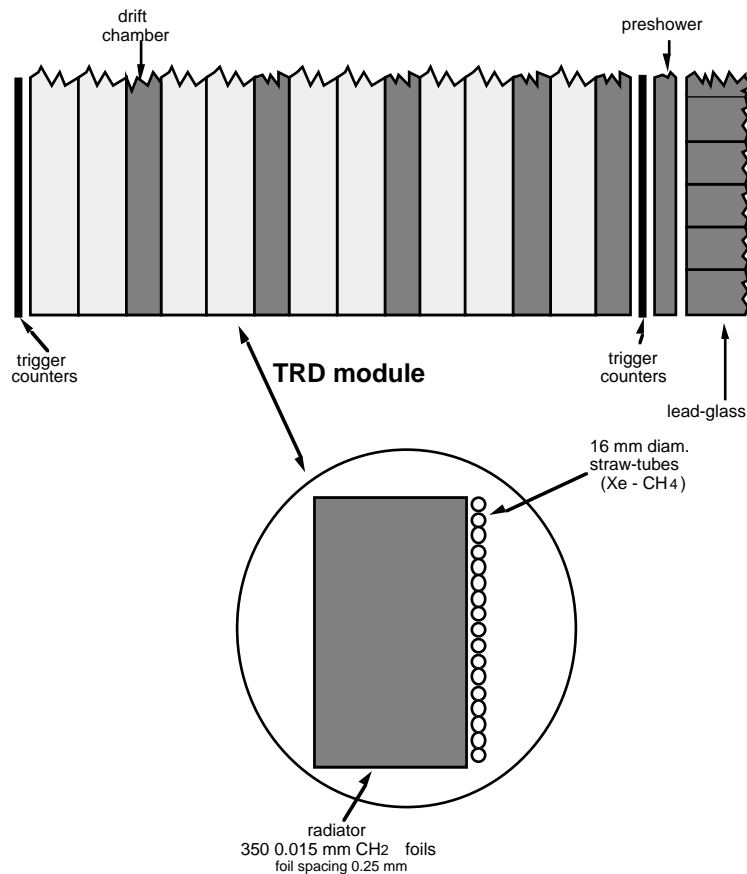

Fig. 24 Details of the NOMAD transition radiation detectors.

A typical neutrino interaction in the NOMAD detector is shown in Fig. 25.

Similar considerations apply to the decay $\tau^- \to \nu_\tau \mu^- \bar{\nu}_\mu$, albeit with a much larger background. This can be reduced to a tolerable level at the expense of detection efficiency by reducing the size of the selected region in the $(\phi_{mh}, \phi_{\mu h})$ plane.
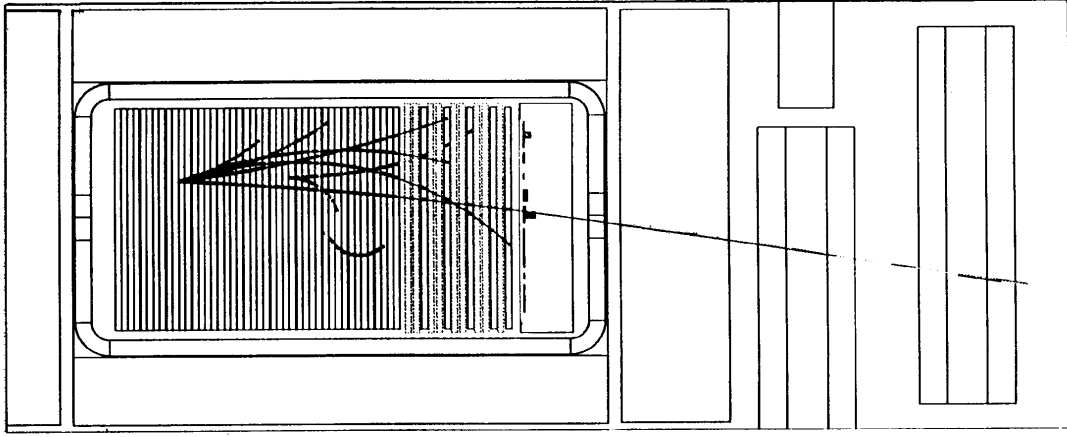
Fig. 25   Typical ν_μ CC event in the NOMAD detector. In addition to the μ^- and to other charged particles produced in the interaction, the event contains a V°, most likely resulting from photon conversion.

The search for the hadronic decay modes $\tau^- \rightarrow \nu_\tau \pi^-$, $\nu_\tau \rho^-$, $\nu_\tau \pi^- \pi^- \pi^+$ is also possible with the NOMAD detector. The main criteria for identifying such decay modes are :

(i)   the presence of a hadronic system consistent with τ^- decay in events with no visible charged lepton;

(ii)   the total momentum vectors of this hadronic system and of all the remaining hadrons in the event must be at opposite azimuthal angles;

(iii)   the transverse components of these two momenta with respect to the nominal beam direction must both exceed a given threshold, typically set at 1.6 GeV.

The sensitivity of NOMAD to ν_μ - ν_τ oscillations for a total of 2.4 x 10^{19} protons on target is listed in Table 5 for the various τ^- decay channels. The background to all these channels, except for $\tau^- \rightarrow \nu_\tau \mu^- \bar{\nu}_\mu$ decay, can be monitored from the data themselves using the very large sample of ν_μ CC events recorded in the experiment (more than 10^6 events in a two-year run). The observation of seven events consistent

with the expected background in the leptonic channels, and of no event in the hadronic channels gives an upper limit $v_\tau/v_\mu < 1.9 \times 10^{-4}$ at the 90% confidence level.
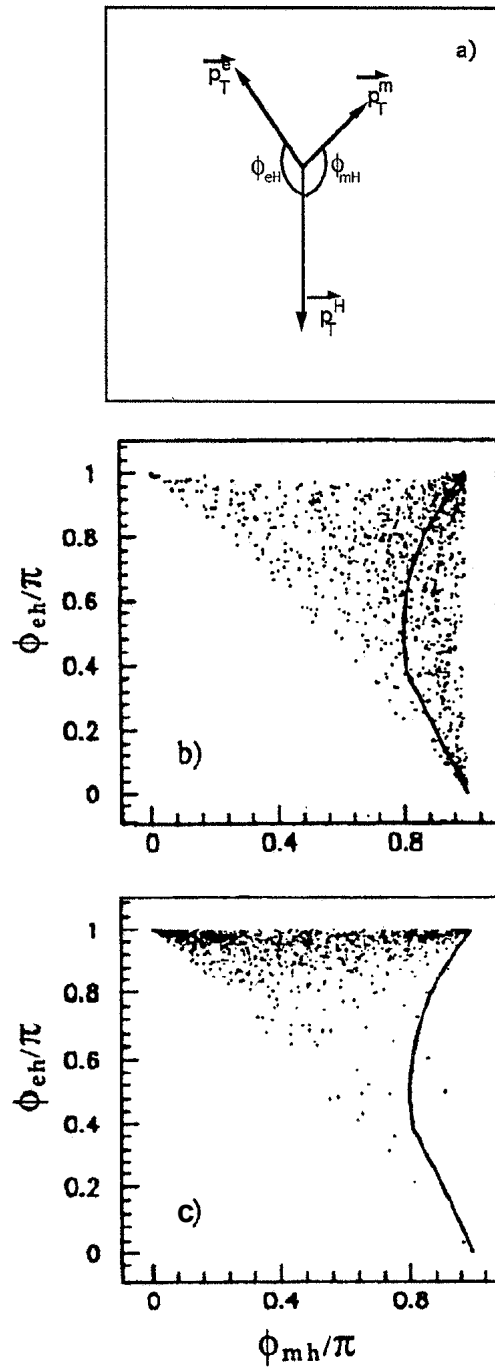

Fig. 26 a) Definition of the azimuthal separations ϕ_{eh} and ϕ_{mh} in terms of transverse momentum vectors;

b) Distribution in the (ϕ_{mh}, ϕ_{eh}) plane for v_τ CC interactions followed by $\tau^- \to v_\tau e^- \bar{v}_e$ decay;

c) the same for ν_e CC interactions. The full line defines the selected region for τ^- events.

TABLE 5

NOMAD sensitivity to ν_τ CC interactions. The number of events corresponds to a run of 2.4×10^{19} protons on target.

$\tau-$ decay mode	Branching ratio	Efficiency	N_τ^*	Background events
$\nu_\tau e^- \bar{\nu}_\mu$	0.0178	0.135	39	4.6
$\nu_\tau \mu^- \bar{\nu}_\mu$	0.0178	0.039	11	2.2
$\nu_\tau \pi^- \pi^- \pi^+ + n\pi^\circ$	0.138	0.077	18	< 0.2
$\nu_\tau \pi^-$	0.11	0.014	3	< 0.2
$\nu_\tau \rho^-$	0.23	0.020	7	< 0.2
Total			78	6.8

For $\Delta m^2 > 40$ eV^2 this corresponds to the limit

$$\sin^2 2\theta < 3.8 \times 10^{-4}$$

Fig. 27 shows the region of the $(\sin^2 2\theta, \Delta m^2)$ plane excluded by the combined CHORUS and NOMAD results if no signal is seen in either experiment. For $\Delta m^2 > 40$ eV^2 the limit on the $\nu_\mu - \nu_\tau$ mixing angle is

$$\sin^2 2\theta < 2.3 \times 10^{-4} \tag{64}$$

which represents an improvement by more than a factor of 20 with respect to the existing limits.
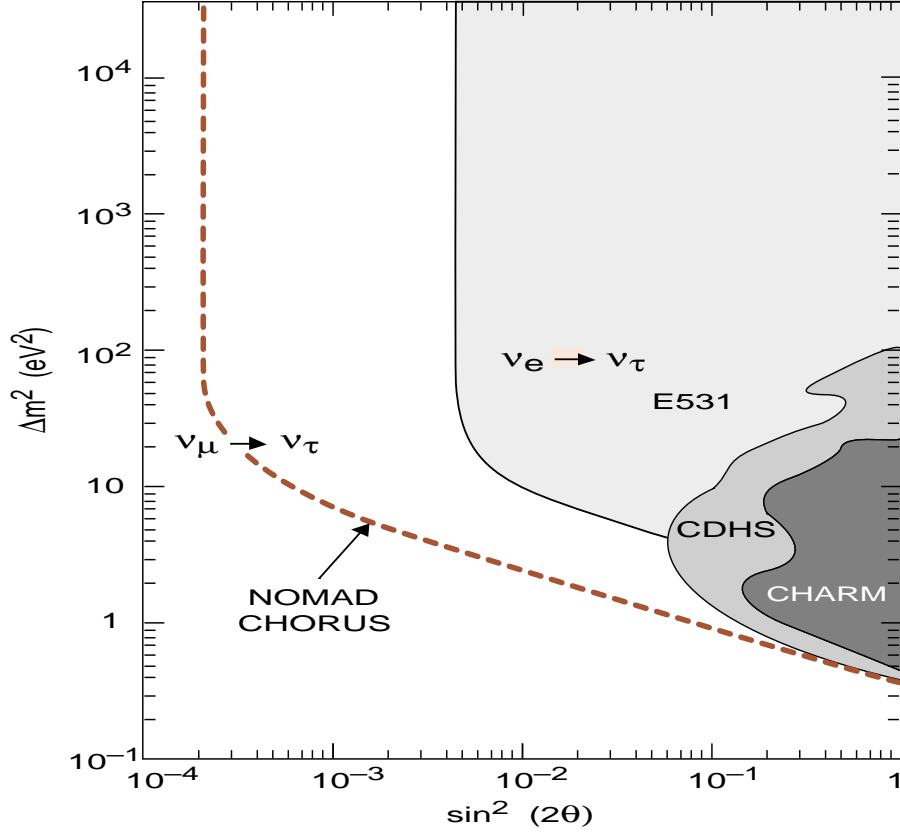
Fig. 27   Region of the ($\sin^2 2\theta$, Δm^2) plane excluded by the combined results of CHORUS and NOMAD if no τ^- signal is observed in either experiment. Also shown are the exclusion regions from previous experiments.

5.   THE ATMOSPHERIC NEUTRINO PROBLEM

Since the total thickness of the atmosphere is $\sim 10^3\,\mathrm{g/cm^2}$, which is equivalent to ~ 10 interaction lengths, the interaction of a primary cosmic ray in the upper layers of the atmosphere results in the development of a hadronic shower leading to a flux of neutrinos from charged pion and muon decay. These neutrinos have energies ranging from ~ 0.1 GeV to few GeV.

Since a ν_μ is produced from both $\pi^\pm$ and μ^+ decay, and a ν_e from $\mu^\pm$ decay only, one expects the ratio between the ν_μ and ν_e fluxes on Earth to be of the order of 2. However, the calculation of the atmospheric neutrino fluxes are affected by sizeable uncertainties which result from uncertainties on the composition and energy spectrum of the primary cosmic rays, on secondary particle distributions and on the

K/π ratio. The final uncertainty affecting the ν_μ and ν_e fluxes on Earth is estimated to be of the order of $\pm\,30\%$ [35]. However, because of partial cancellations, the uncertainty on the predicted ν_μ/ν_e ratio is believed to be less than $\pm\,10\%$.

Five underground experiments have measured the atmospheric neutrinos fluxes by detecting quasi-elastic interactions :

$$\nu_\mu\,(\nu_e\,) + n \rightarrow \mu^-\,(e^-\,) + p \tag{65a}$$

$$\overline{\nu}_\mu(\overline{\nu}_e) + p \rightarrow \mu^+\,(e^+) + n \tag{65b}$$

Two experiments (KAMIOKANDE [36] and IMB-3 [37]) are based on large volume water tanks and detect the Čerenkov light ring produced by relativistic particles in the water. The other three experiments (FREJUS [38], NUSEX [39] and SOUDAN-2 [40]) use calorimeters with high longitudinal and transverse segmentation.

Muons from reactions (65a) and (65b) appear in all these detectors as single penetrating tracks. If the muon stops in the detector and decays, the decay electron can also be observed.

Electrons produce single electromagnetic showers consisting of many short tracks which are easily identified in the calorimeters and result in diffuse Čerenkov light rings in KAMIOKANDE and IMB-3.

The comparison between the measured and predicted $\nu_\mu\,/\nu_e$ ratio for the five experiments is shown in Table 6. The average of the five results, after adding the statistical and systematic errors in quadrature, is

$$\frac{\left(\nu_\mu\,/\,\nu_e\right)_{\text{measured}}}{\left(\nu_\mu\,/\,\nu_e\right)_{\text{predicted}}} = 0.61 \pm 0.06 \tag{66}$$

The deviation of this ratio from 1 illustrates the so-called atmospheric neutrino problem.

Table 6

Comparison between the measured and calculated ν_μ / ν_e ratio for atmospheric neutrinos. The second error shows separately the uncertainty on the calculation.

Experiment		Detector mass x years of exposure	$\dfrac{\left(\nu_\mu / \nu_e\right)_{measured}}{\left(\nu_\mu / \nu_e\right)_{predicted}}$
KAMIOKANDE	[36]	6.1	$0.60 \pm 0.07 \pm 0.05$
IMB-3	[37]	7.7	$0.54 \pm 0.05 \pm 0.07$
FREJUS	[38]	1.6	0.87 ± 0.21
NUSEX	[39]	0.4	0.99 ± 0.40
SOUDAN-2	[40]	1.0	$0.69 \pm 0.19 \pm 0.09$

A comparison of the ν_μ and ν_e fluxes, as measured by KAMIOKANDE [36,41], with the calculated fluxes is shown in Fig. 28. It appears from this comparison that the ν_μ flux is lower than predicted while the ν_e flux agrees with calculations. This could just be the effect of the large uncertainties affecting these calculations. However, an interpretation of these results in terms of neutrino oscillations is also possible. In this case, ν_μ - ν_τ and ν_μ - ν_e oscillations are both acceptable solutions. For ν_μ - ν_e oscillations, since the ratio ν_μ / ν_e is close to 2 at production, the ν_μ flux on Earth is reduced despite the fact that the two probabilities $P(\nu_\mu \rightarrow \nu_e)$ and $P(\nu_e \rightarrow \nu_\mu)$ are equal (see Section 1). For ν_μ - ν_τ oscillations, the energy threshold for τ^- production in quasi-elastic neutrino scattering is 3.5 GeV, hence for energies below this value the ν_τ is not detected.

Additional evidence in favour of neutrino oscillations has been recently reported by KAMIOKANDE [41]. Since the flux of atmospheric neutrinos on Earth is, to a good approximation, isotropic, the neutrino flight path from the production point to the detector varies enormously with the zenith angle θ. For example,

neutrinos impinging on the detector from above ($\cos\theta = 1$) are produced few kilometres above the detector, while upward going neutrinos ($\cos\theta = -1$) have traversed the Earth and so have travelled for at least 13, 000 km before reaching the detector. Hence, depending on Δm^2, oscillations may result in a dependence of the ν_μ/ν_e ratio on the zenith angle θ.
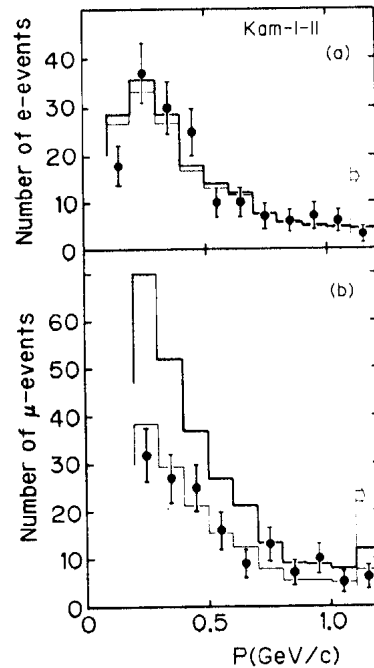

Fig. 28   Momentum spectrum of electrons (a) and muons (b) from quasi-elastic scattering of atmospheric neutrinos, as measured by KAMIOKANDE. The histograms show the predictions without neutrino oscillations (thick line) and with neutrino oscillations (thin line).

Such a measurement is only possible in the case of multi-GeV neutrinos, for which the outgoing lepton direction is correlated with the incident neutrino direction (on average, the angle between the outgoing lepton and the incident neutrino has a r.m.s. deviation from zero of ~ 60° for energies below 1 GeV, and of less than 20° for energies above 1.5 GeV).

The variation of the ν_μ/ν_e flux ratio with zenith angle with respect to the predictions in the absence of oscillations, as reported by KAMIOKANDE [41], is

shown in Fig. 29. Within the limited statistics, these data are consistent with a reduction of the ν_μ/ν_e ratio at large flight distances.
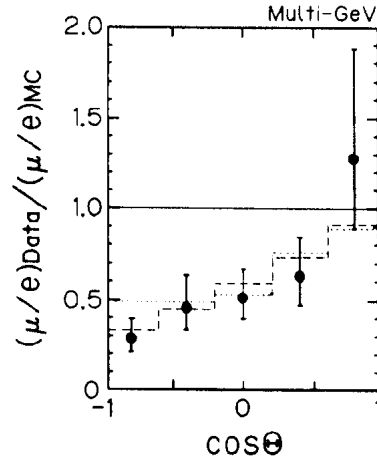

Fig. 29   Zenith angle distribution of the ratio between the number of μ^- and e^- events, as measured by KAMIOKANDE, normalized to the predicted ratio in the absence of oscillations . The histograms are expectations from ν_μ - ν_e oscillations with $\Delta m^2 =$ 0.018 eV^2 (dashed line) or ν_μ - ν_τ oscillations with $\Delta m^2 = 0.016$ eV^2 (dotted line). For both cases $\sin^2 2\theta = 1$ is assumed.

When interpreted in terms of ν_μ - ν_τ oscillations, these results favour a large mixing angle solution ($\sin^2 2\theta \geq 0.6$) and $\Delta m^2 \approx 0.016$ eV^2.

If these are indeed the parameters describing ν_μ - ν_τ oscillations, it can be seen from Eq. (10) that the probability for ν_τ appearance in a ~ 30 GeV ν_μ beam is maximal at a distance of ~ 3700 km from the source. As a consequence, for the CHORUS and NOMAD experiments, which are located at a distance of ~ 0.8 km from the neutrino source, the probability of τ appearance is negligibly small (of the order of 5×10^{-7}) and no oscillation signal can be detected in those experiments.

6.   RECENT SEARCHES FOR ν_μ - ν_e OSCILLATIONS AT ACCELERATORS

6.1   The LSND experiment

The Liquid Scintillator Neutrino Detector (LSND) has recently reported the observation of events which can be interpreted in terms of ν_μ - ν_e oscillations [42].

The LSND experiment uses neutrinos from π and μ decay from the beam stop of the Los Alamos Meson Physics Facility (LAMPF). The layout of the experiment is shown in Fig. 30. Protons from the LAMPF 800 MeV linear accelerator produce pions in a 30 cm long water target located $\sim$ 1 m upstream of a copper beam stop. Neutrinos are produced by the following decay processes :

(i) $\quad \pi^+ \rightarrow \mu^+ \nu_\mu$ (in flight or at rest);

(ii) $\quad \mu^+ \rightarrow e^+ \bar{\nu}_\mu \nu_e$ (at rest);

(ii) $\quad \pi^- \rightarrow \mu^- \bar{\nu}_\mu$ (in flight);

(iv) $\quad \mu^- \rightarrow e^- \nu_\mu \bar{\nu}_e$ (at rest).
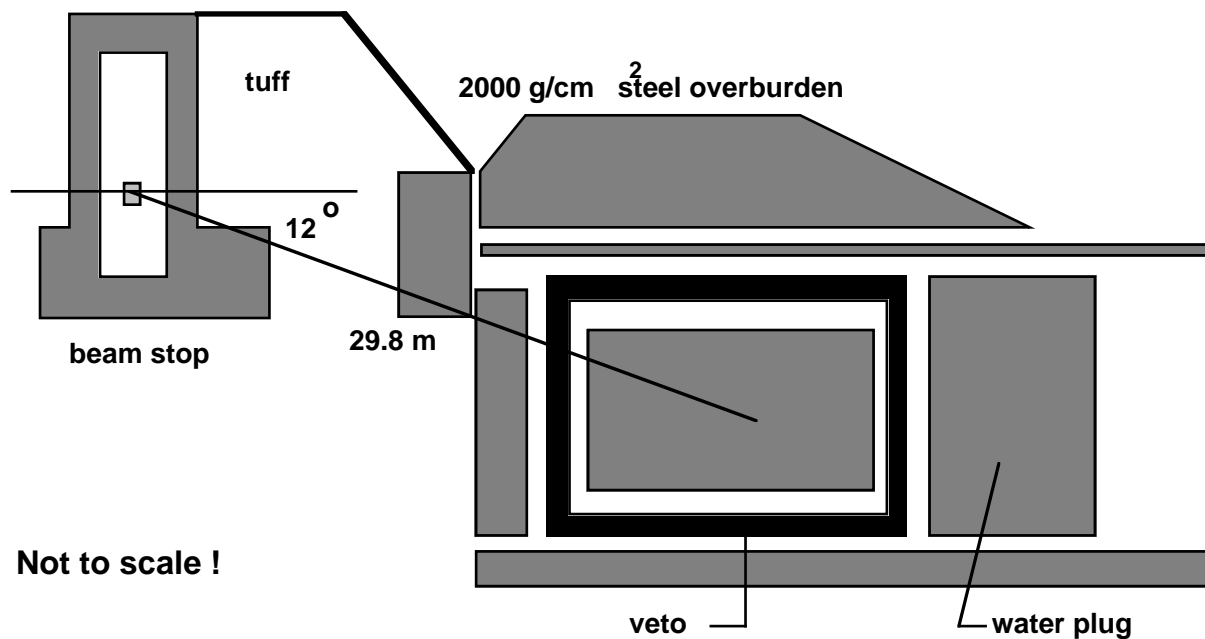

Fig. 30 Sketch of the LSND experiment.

The relative yield of $\bar{\nu}_e$ above an energy of 36 MeV is only $\sim 4 \times 10^{-4}$ because π^- decaying in flight are only a few % of all produced π^- and only a small fraction of the μ^- stopping in high Z material undergoes decays (π^- at rest do not decay because they are immediately captured by nuclei).

LSND consists of a tank containing 167 tonnes of liquid scintillator (doped mineral oil, CH_2). Both scintillation and Čerenkov light are collected by 1220 photomultipliers covering 25% of the tank surface. The tank itself is inside a liquid scintillator shield which is used in anticoincidence to reject charged particles entering the tank from outside.

LSND detects $\bar{\nu}_e$ by the reaction

$$\bar{\nu}_e + p \rightarrow e^+ + n \tag{67}$$
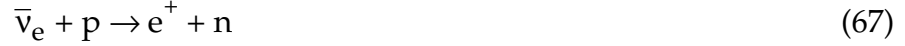
which gives a prompt e^+ signal followed by a delayed 2.2 MeV γ-ray from the capture reaction $np \rightarrow d\gamma$.

A total of nine events has been observed in the e^+ energy interval from 36 to 60 MeV during two runs in 1993-94, to be compared with an expected background of 2.12 ± 0.34 events [42]. The probability that the excess of 6.9 events results from a statistical fluctuation is $<10^{-3}$. If attributed to $\bar{\nu}_\mu - \bar{\nu}_e$ oscillations, this excess corresponds to an oscillation probability of $\left(0.34 \, ^{+0.20}_{-0.18} \pm 0.07 \right) \times 10^{-2}$.

However, an independent analysis of the same data [43] reports the observation of only five events, to be compared with an estimated background of 6.2 events. In this analysis it is found that the beam-on e^+ signals are not uniformly distributed over the detector volume but are concentrated near the bottom edge. The use of a fiducial volume cut to remove this region leads to a result consistent with no oscillations.

Fig. 31 displays the LSND allowed region in the $\sin^2 2\theta$, Δm^2 plane under the assumption that the positive signal reported in ref. [42] is due to $\bar{\nu}_\mu - \bar{\nu}_e$ oscillations, together with the regions excluded by the alternative LSND analysis [43] and by other experiments.
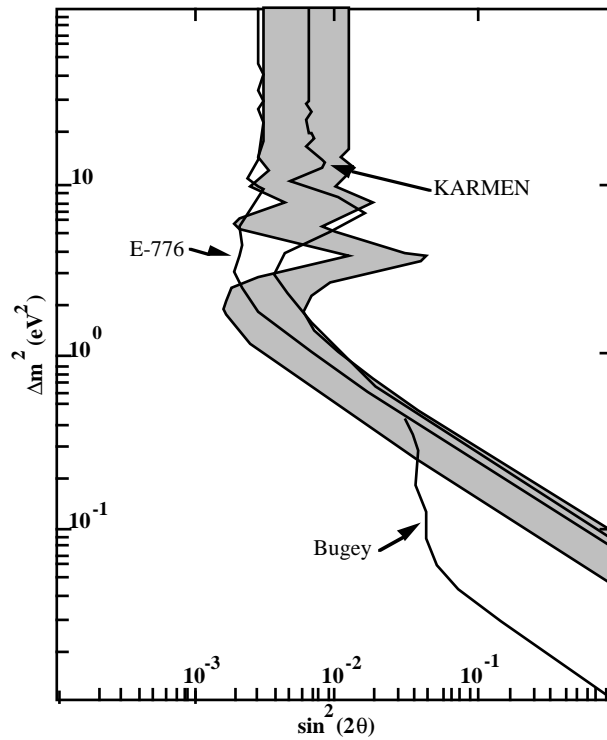
Fig. 31   Region of the $\sin^2 2\theta$, Δm^2 plane allowed by LSND (shaded area) together with the exclusion regions from a previous BNL experiment (E-776 [46]), from KARMEN [45] and from the Bugey reactor experiment (B. Achtar et al. [3]). The alternative LSND analysis [43] gives a limit similar to KARMEN [45].

6.2   The KARMEN experiment

The KArlsruhe-Rutherford Medium Energy Neutrino (KARMEN) experiment [44] is being performed at the spallation neutron facility ISIS of the Rutherford-Appleton Laboratory.

The layout of the experiment is shown in Fig. 32. A proton beam with a kinetic energy of 800 MeV bombards the ISIS target producing pions which are stopped in the target shielding resulting in a neutrino beam similar to the LAMPF one. However, an important difference with respect to LAMPF is that the ISIS beam is pulsed with a time structure consisting of two 100 ns long pulses separated by 320 ns (this sequence has a repetition rate of 50 Hz). Thus it is possible to separate neutrinos from muon and pion decay from their different time distributions with respect to the beam pulse.
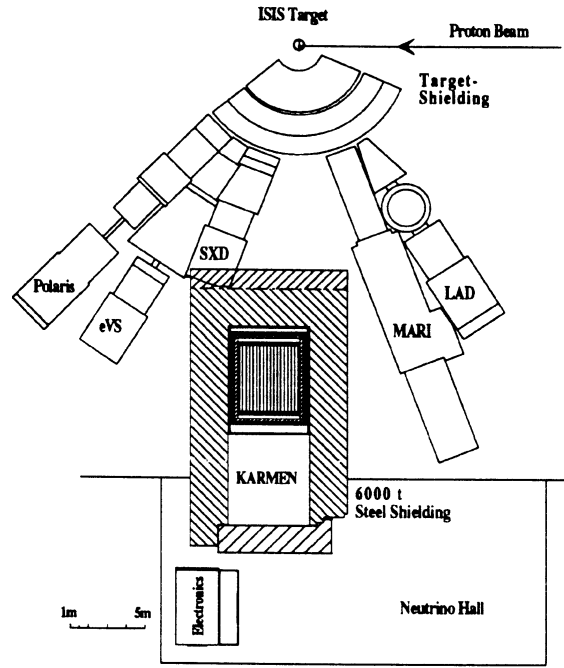
Fig. 32 Layout of the KARMEN experiment.

The KARMEN detector consists of 56 tonnes of liquid scintillator contained in a matrix of 512 independent 3.5 m long boxes with a section of 18 x 18 cm^2 and viewed by two photomultipliers at each end. A thin layer of Gd_2O_3 placed between adjacent boxes allows neutron detection by neutron capture in Gadolinium followed by γ emission. The advantages of this technique with respect to neutron capture from protons is that the cross-section is large for fast neutrons, hence one can use faster coincidences. In addition, the total γ-ray energy is ~ 8 MeV.

The KARMEN experiment has observed no signal above the expected background from reaction (67), providing no evidence for v_μ - v_e oscillations [45].

The regions of the $\sin^2 2\theta$, Δm^2 plane excluded by the KARMEN experiment [45] and by earlier experiments are shown in Fig. 31. A small region with 0.3 $eV^2 < \Delta m^2 <$ 2 eV^2 and $\sin^2 2\theta$ in the range 0.04 to 0.002 (depending on Δm^2) is compatible with the positive result of ref. [42] without being excluded by the other ones. However, in view of the limited statistical evidence of the LSND experiment and of the existence of an independent analysis reaching different conclusions, it is not possible at

present to consider the LSND result [42] as evidence for ν_μ - ν_e oscillations. More data are needed to reach a definitive conclusion.

It is quite difficult to explain the LSND result [42] as well as the solar and atmospheric neutrino problems in terms of oscillations involving three neutrino flavours because three very different values of Δm^2 are required by the data whereas with three neutrinos only two independent values of Δm^2 can be defined.

7. FUTURE OSCILLATION SEARCHES

7.1 Short base-line experiments at accelerators

A new search for ν_μ - ν_τ oscillations has been recently approved at Fermilab. This experiment, named COSMOS, uses the neutrino beam which will become available at Fermilab near the end of the century when the new Main Injector (MI) will start operation.

The COSMOS experiment [47] is conceptually similar to CHORUS. The apparatus is shown in Fig. 33. The neutrino target consists of 520 kg of emulsion followed by a high-precision scintillating fibre tracker, an open gap dipole magnetic spectrometer with a field of 0.5 T.m, drift chambers, an electromagnetic calorimeter and a muon detector. The two main differences with respect to CHORUS are a more intense neutrino beam and the magnetic spectrometer which provides a better momentum resolution ($\sigma_p/p \approx 3\%$, to be compared with ~ 20% for the CHORUS hexagonal magnet). This latter property should provide a stronger reduction of the number of events to be scanned in the emulsion, thus allowing for a much larger number of neutrino interactions while keeping the scanning time within a reasonable limit.

Table 7 compares the main parameters of the future Fermilab Main Injector and neutrino beam with those presently available from the CERN SPS. It must be pointed out that the cross-section for τ^- production from ν_τ's in the neutrino beam from the Fermilab Main Injector is a factor of ~ 5 lower than in the CERN beam because of the lower energy of the interacting neutrinos.
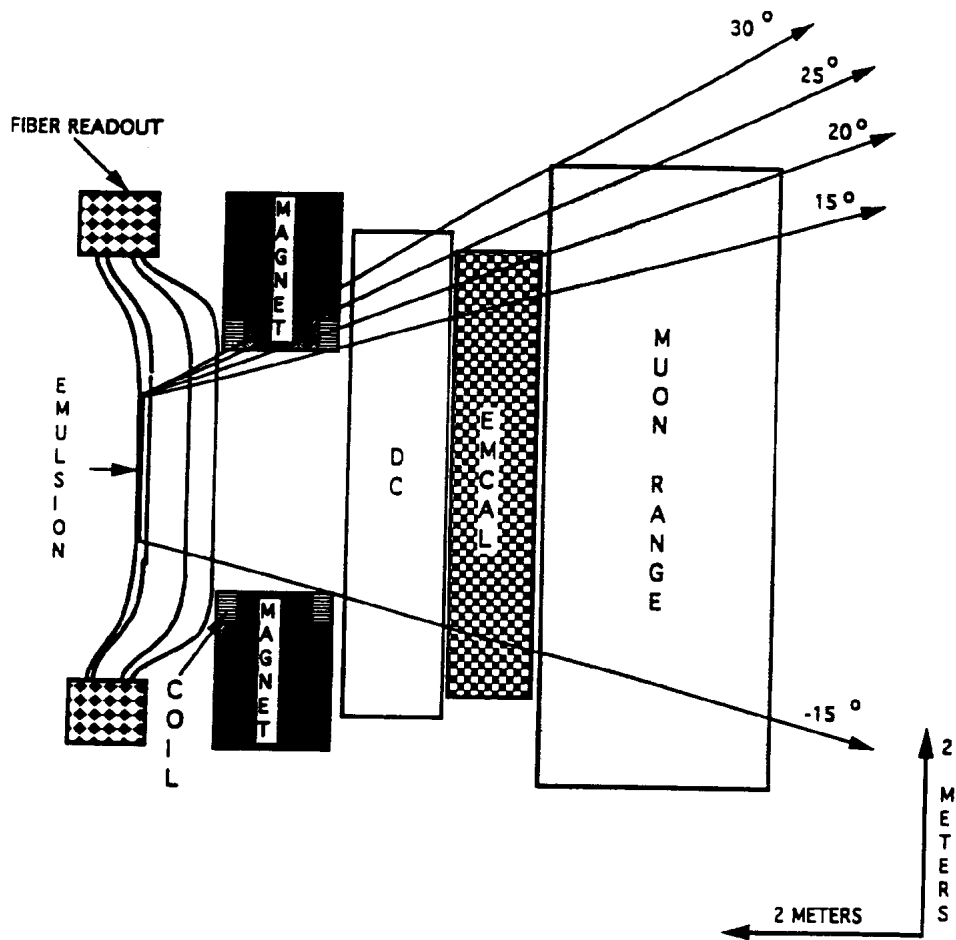
Fig. 33 Side-view of the COSMOS detector.

Table 7

List of relevant beam parameters.

	CERN SPS	Fermilab MI
Proton energy	450 GeV	120 GeV
Protons on target/cycle	2×10^{13}	6×10^{13}
Cycle time	14.4 s	1.9 s
Protons on target/year	1.2×10^{19}	3×10^{20}
Average energy of interacting ν_μ	40 GeV	16 GeV

COSMOS will start data taking around the year 2000. It expects to collect 6.3 x

10^6 ν_μ CC events in a run of four years. The corresponding number of events to be

scanned is $\sim 1.5 \times 10^5$. Fig. 34 shows the region of the $\sin^2 2\theta$, Δm^2 plane which will be excluded by COSMOS if no oscillation signal is observed. It will improve the anticipated CHORUS and NOMAD limit by an order of magnitude.
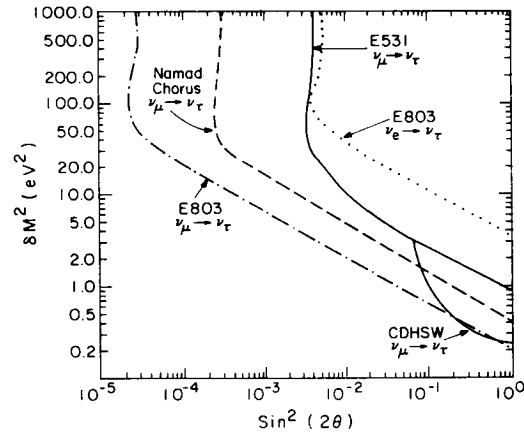

Fig. 34   Region of the $\sin^2 2\theta$, Δm^2 plane excluded by COSMOS after a four-year run if no ν_τ signal is observed. Also shown is the anticipated limit from CHORUS and NOMAD, together with limits from previous experiments.

7.2   Long base-line experiments at accelerators

If the atmospheric neutrino problem discussed in section 5 is indeed the result of neutrino oscillations, then the value of $\Delta m^2 \approx 10^{-2}$ eV^2 needed to explain the data will give rise to oscillations which can be detected by installing a suitable detector at a distance of the order of 1000 km from a source of neutrinos with energies of the order of 10 GeV.

The future neutrino programme at Fermilab includes a long base-line experiment. The neutrino beam from the Main Injector is directed towards the Soudan underground laboratory in Minnesota at a distance of 730 km from Fermilab (see Fig. 35).

Fig. 35 Future neutrino beam-line from Fermilab to Soudan.

The Soudan laboratory, at a depth of 713 m (2090 m of water equivalent), will be equipped with a new underground hall oriented along the neutrino beam where the Main Injector Neutrino Oscillation Search (MINOS) will be installed.

The MINOS detector [48] is shown in Fig. 36. It consists of 600 octagonal magnetized iron plates, 4 cm thick, interleaved with active detector planes providing at the same time calorimetric and tracking information. The total mass of the MINOS detector is 10,000 tonnes. With such a mass and a wide-band beam, one expects approximately 20,000 ν_μ CC events per year.

The MINOS detector is used in conjunction with a second detector of similar conceptual design but with a much smaller mass located at a distance of ~ 1 km from the proton target.

MINOS uses several methods to detect ν_μ - ν_τ oscillations. One method consists of measuring the ratio of the number of events with no muon to the number of events with one muon. If ν_μ - ν_τ oscillations are present with the oscillation parameters suggested by the atmospheric neutrino problem, this ratio will be different for the far and near detector because only ~ 18% of the ν_τ CC events will produce a μ^- from $\tau^- \rightarrow \nu_\tau \mu^- \bar{\nu}_\mu$ decay.

MINOS (Main Injector Neutrino Oscillation Search)
Far (Labyrinth) Detector
Fermilab

32,000 m^2 Active Detector Planes
x and y strip/wire readout
480,000 channels

$\vec{B}$

36 m

8m

Magnetized Fe Plates
600 Layers x 4 cm Fe
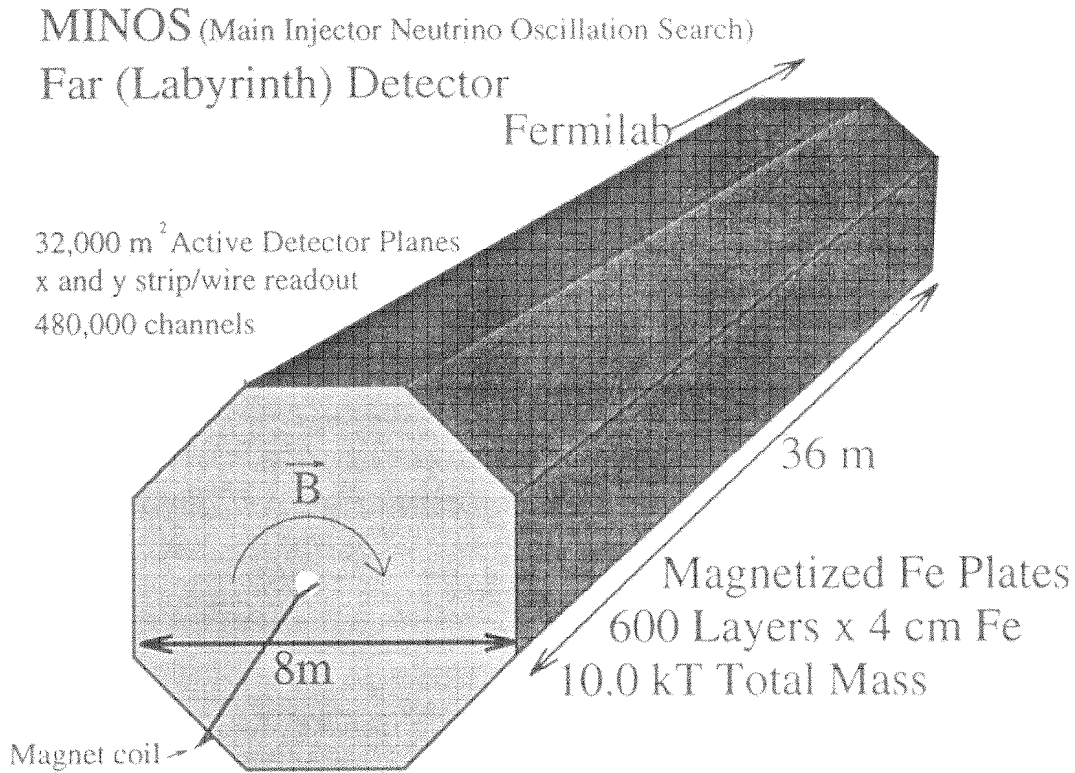10.0 kT Total Mass

Magnet coil

Fig. 36 Sketch of the MINOS detector.

An alternative, independent method consists in measuring the neutrino energy spectrum in both the far and near detector by measuring the total visible energy in events containing a μ^-. The presence of ν_μ - ν_τ oscillations would then result in a distortion of the spectrum measured in the far detector with respect to the spectrum measured in the near detector. Using Eq. (10), the shape of this distortion will provide a determination of the oscillation parameters.

MINOS will begin data taking at the beginning of the next century in parallel with the short base-line COSMOS experiment described previously. It will be able to demonstrate the presence of ν_μ oscillations for mixing angles $\sin^2 2\theta > 0.01$ and for $\Delta m^2 > 10^{-3} eV^2$.

Another possibility for long base-line neutrino oscillation searches, now being actively discussed in Europe, consists in aiming a neutrino beam from the CERN SPS to the Gran Sasso National Laboratory in Italy at a distance of 732 km. The three

existing underground halls at Gran Sasso, under ~ 4000 m of water equivalent, are already oriented towards CERN and ICARUS, a 600 tonnes detector suitable for oscillation searches, will start operation in 1998 with the main goals of searching for proton decay and of studying atmospheric and solar neutrinos.

ICARUS [49] is a new detector concept based on a liquid Argon Time Projection Chamber (TPC) which allows three-dimensional reconstruction of events with spatial resolution of the order of 1 mm. The principle of this detector is illustrated in Fig. 37.
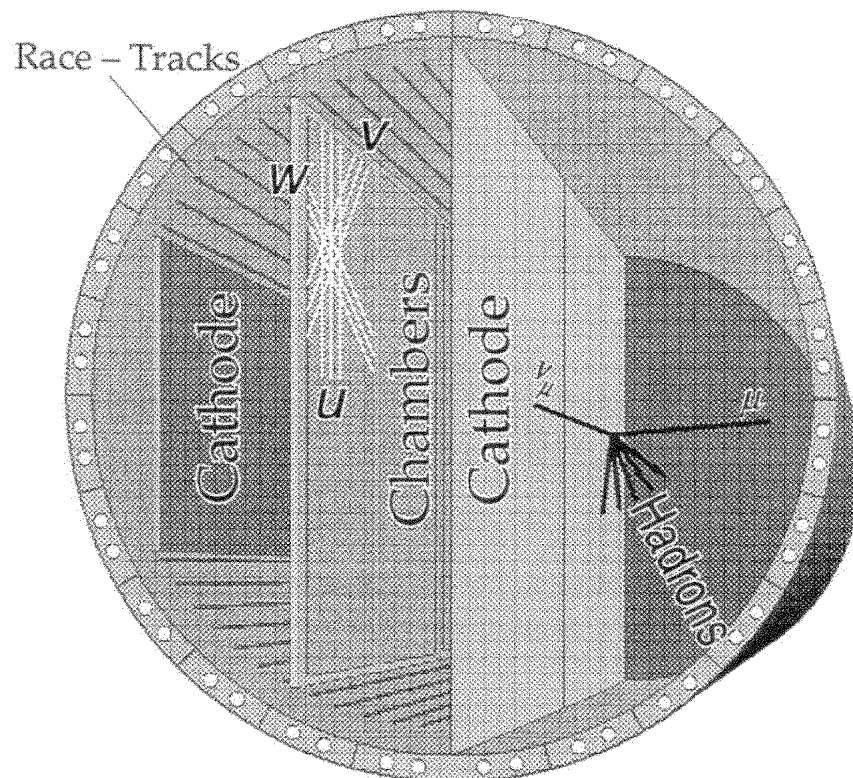

Fig. 37   Principle of the ICARUS detector. The drift direction is perpendicular to the cathode and chamber planes.

Primary ionisation electrons drift in very high purity liquid Argon over distances of the order of 1 m and are collected by electrodes made of strips which provide two of the three coordinates and measure the ionisation, while the third coordinate along the drift direction is determined by measuring the drift time.

After one year of data taking using a wide-band neutrino beam from the CERN SPS ICARUS should be able to exclude neutrino oscillations with $\Delta m^2 > 2 \times 10^{-2} eV^2$

and $\sin^2 2\theta > 0.1$ if no signal is observed. The exclusion region should extend to Δm^2 values as low as 3×10^{-3} eV^2 for larger mixing angles.

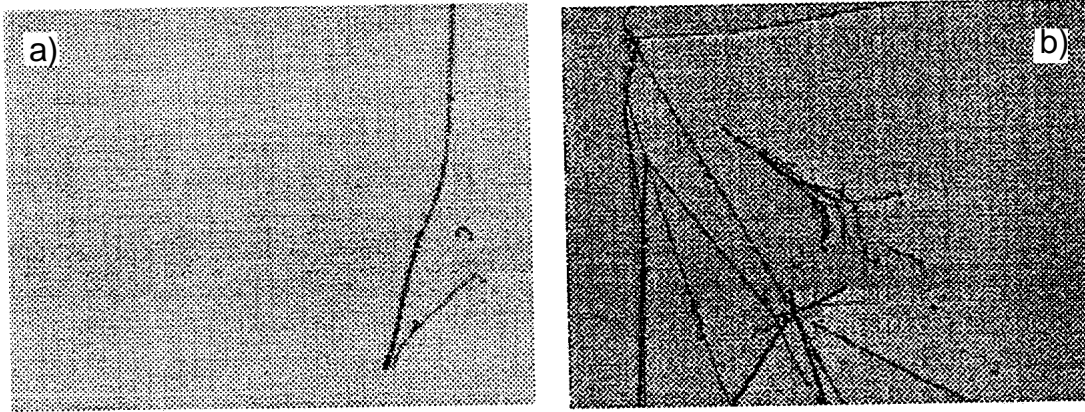Fig. 38 shows the track quality achieved in a 3 tonnes prototype.

Fig. 38a) Stopping cosmic ray muon with delayed decay electron;

b) Hadronic shower from a cosmic ray. A photon produces an electromagnetic shower near the centre of the picture.

7.3   Experiments on solar neutrinos

7.3.1 SNO

The Sudbury Neutrino Observatory (SNO) is a solar neutrino detector under construction in the Creighton mine near Sudbury, Ontario [50]. The detector, located 2070 m below ground (5900 m of water equivalent), consists of a spherical vessel with a radius of 6 m   containing ~ 1000 tonnes of high purity heavy water. Čerenkov light produced in the heavy water is collected by 9600 photomultipliers with a diameter of 20cm located on a concentric spherical surface at a radius of 8.5 m. About 7000 tonnes of high purity light water shield the heavy water against radioactivity from the walls of the laboratory.

Solar neutrinos are detected by the observation of the reactions

$$\nu_e + d \rightarrow p + p + e^- \qquad\qquad (68a)$$

$$\nu + e^- \rightarrow \nu + e^- \qquad\qquad (68b)$$
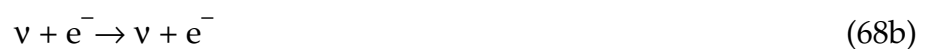
For both reactions, the Čerenkov light ring produced by the electron is detected with a threshold of ~ 2 MeV, which makes the experiment sensitive only to neutrinos from B^8 decay (see Eq. 19h and Fig. 4). Reaction (68a) has the advantage of a much larger cross-section with respect to reaction (68b) but the disadvantage that the electron direction is practically uncorrelated with the incident neutrino direction.

An additional feature of SNO is its anticipated capability to detect the reaction

$$v + d \rightarrow p + n + v \tag{68c}$$

which has the same cross-section for all neutrino flavours and measures, therefore, the total solar neutrino flux. This reaction is observed by dissolving high purity $MgCl_2$ salt into the heavy water and by detecting the 8.5 MeV γ-ray emitted by neutron capture in Cl^{35}:

$$n + Cl^{35} \rightarrow Cl^{36} + \gamma$$
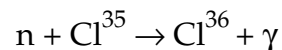
As the detector does not distinguish between electrons and photons, it is planned to alternate data taking runs with and without $MgCl_2$ salt. Another possibility being actively studied is the insertion of special neutron counters in the vessel.

SNO is expected to start data taking in 1997. In the absence of oscillations, one expects ~ 10^4 events/year from reaction (68a), ~ 10^3 events/year from reaction (68b) and ~ 3×10^3 events/year from reaction (68c) with $MgCl_2$ salt. The presence of v_e oscillations reduces the event rates from reactions (68a) and (68b) but does not change the rate of reaction (68c).

7.3.2 BOREXINO

BOREXINO is an experiment presently under construction at the Gran Sasso National Laboratory [51]. The detector consists of a spherical, transparent vessel of 8.5 m diameter filled with very high purity, low activity liquid scintillator and

viewed by an array of 1650 photomultipliers located on its surface. The relative timing of the photomultiplier signals provides information of the event position within the detector volume. The entire detector is immersed in a cylindrical tank 16.5 m high with a 16.5 m diameter filled with high purity water and acting as a shield.

The aim of the experiment is to detect the ν_e - electron scattering reaction (68b) with an energy threshold as low as 0.25 MeV. If this is achieved, the experiment is sensitive to the ν_{Be} component (E = 0.861 MeV) which is expected to be strongly suppressed if neutrino oscillations are the solution of the solar neutrino problem (see section 3.5). In the absence of oscillations one expects a contribution of ~ 50 events/day from these neutrinos. With such a rate, it is possible to identify the solar origin of the signal by observing the ~ 7% yearly variation associated with the varying distance between the Sun and the Earth.

BOREXINO is expected to start data taking sometime after the beginning of 1998.

7.4   Experiments at nuclear reactors.

Two $\overline{\nu}_e$ disappearance experiments are presently under construction at the Chooz (France) and San Onofre (California) nuclear power plants [52].

The Chooz detector , installed in an underground tunnel at a distance of 1025 m from the reactors, consists of three concentric vessels. The innermost one contains 4.9 tonnes of Gadolinium doped liquid scintillator which acts as the $\overline{\nu}_e$ target and as the detector. The two other vessels are both filled with liquid scintillator. The outermost vessel is used as an active veto and as a shield.

The San Onofre detector, installed at 750 metres from two reactors, consists of 12 tonnes of Gadolinium loaded liquid scintillator surrounded by 1 metre thick water shield and by a liquid scintillator layer to reject cosmic rays. The central detector is subdivided into 66 independent cells.

In both experiments the reaction $\overline{\nu}_e p \rightarrow e^+ n$ produces a prompt e^+ signal followed by a delayed photon signal resulting from neutron capture in Gadolinium. In the Chooz detector the middle vessel is used to increase the photon detection

efficiency. In the San Onofre detector the e^+ and the two photons from e^+ annihilation are detected in three neighbouring cells.

These experiments are sensitive to $\bar{\nu}_e$ oscillations with Δm^2 values in the range from 3×10^{-3} to 3×10^{-2} eV^2 and $\sin^2 2\theta > 0.1$.

7.5   SUPER-KAMIOKANDE

SUPER-KAMIOKANDE is a new, very massive water Čerenkov detector [53]. The total mass of water is 50,000 tonnes, of which 22, 000 tonnes represent the fiducial volume for solar neutrino detection (in KAMIOKANDE the fiducial volume mass is only 680 tonnes). The Čerenkov light is collected by 11,200 photomultipliers.

SUPER-KAMIOKANDE will study solar and atmospheric neutrinos and will also serve for a long baseline oscillation experiment using a wide-band neutrino beam from the KEK 12 GeV proton synchrotron at a distance of 250 km.

SUPER-KAMIOKANDE should start data taking in the second half of 1996. The expected solar neutrino event rate is ~ 30/day which is two orders of magnitude larger than the corresponding KAMIOKANDE rate. One also expects ~ 2,000 events/year from atmospheric neutrinos.

8.   CONCLUSIONS

Experiments on solar and atmospheric neutrinos have been the only ones so far to provide serious hints for neutrino oscillations. Unfortunately, the source of these neutrinos is not under control and cannot be directly monitored as in the case of reactor or accelerator experiments. While the oscillation parameters which explain the solar neutrino problem cannot be verified using other kinds of neutrino sources, the interpretation of the atmospheric problem in terms of oscillations can be verified in long baseline experiments with neutrino beams of well known properties from accelerators or nuclear reactors.

A wide programme of oscillation searches is presently being carried out or being prepared, together with second-generation experiments on solar neutrinos. Hopefully by the turn of the century it should be clear if neutrino oscillations do indeed occur.

REFERENCES

1. B. Pontecorvo, Sov. Phys. JETP 26 (1968) 984.

2. Z. Maki, M. Nakagawa and S. Sakata, Prog. Theor. Phys. 28 (1962) 870.

3. G. Zacek et al., Phys. Rev. D34 (1986) 2621;

   Z. D. Greenwood, Proc. of the Leptonic Session of the 22nd "Rencontre de Moriond" (1987) 403;

   A. I. Afonin et al., JETP 67 (1988) 213;

   J. Bouchez, Proc. 13th Int. Conference on Neutrino Physics and Astrophysics, Boston (1988) 28;

   S. N. Ketov et al., JETP Lett. 55 (1992) 564;

   G. S. Vidyakin et al., JETP Lett. 59 (1994) 364;

   B. Achtar et al., Nucl. Phys. B434 (1995) 503.

4. F. Dydak et al., Phys. Lett. 134B (1984) 281;

   F. Bergsma et al., Phys. Lett. 142B (1984) 103;

   I. E. Stockdale et al., Z. Phys. C27 (1985) 53.

5. See the review article by F. Vannucci, Proc. 13th Int. Conference on Neutrino Physics and Astrophysics, Boston (1988) 46; see also S. Bilenky, Lepton mixing, in Neutrino Physics, edited by K. Winter, Cambridge University Press (1991), 195.

6. N. Ushida et al., Phys. Rev. Lett. 57 (1986) 2928.

7. Review of Particle Properties, Phys. Rev. D50 (1994) 1234.

8. J. N. Bahcall, Rev. Mod. Phys. 50 (1978) 881;

   J. N. Bahcall, Rev. Mod. Phys. 59 (1987) 505;

   J. N. Bahcall and R. K. Ulrich, Rev. Mod. Phys. 60 (1988) 297;

   J. N. Bahcall, Neutrino Astrophysics, Cambridge University Press (1989).

9. R. Davis, Prog. Part. Nucl. Phys. 32 (1994) 13;

   B. T. Cleveland et al., Nucl. Phys. B (Proc. Suppl.) 38 (1995) 47.

10. J. N. Bahcall and M. H. Pinsonneault, Rev. Mod. Phys. 64 (1992) 885.

11. S. Turck-Chièze and I. Lopes, Astrophys. J. 408 (1993) 347.

12. K. S. Hirata et al., Phys. Rev. Lett. 63 (1989) 6;

    K. S. Hirata et al., Phys. Rev. Lett. 65 (1990) 1297;

    K. S. Hirata et al., Phys. Rev. Lett. 65 (1990) 1301;

    K. S. Hirata et al., Phys. Rev. D44 (1991) 2241;

    Y. Suzuki, Nucl. Phys. B (Proc. Suppl.) 35 (1994) 273;

    Y. Suzuki, Nucl. Phys. B (Proc. Suppl.) 38 (1995) 54.

13. V. A. Kuzmin, Sov. Phys. JETP 22 (1966) 1050.

14. P. Anselmann et al., Phys. Lett. B285 (1992) 376;

    P. Anselmann et al., Phys. Lett. B327 (1994) 377;

    P. Anselmann et al., Nucl. Phys. B (Proc. Suppl.) 38 (1995) 68.

15. P. Anselmann et al., Phys. Lett. B342 (1995) 440;

16. A. I. Abazov et al., Nucl. Phys. B (Proc. Suppl.) 19 (1991) 84;

    A. I. Abazov et al., Phys. Rev. Lett. 67 (1991) 3332;

    V. N. Gavrin, Proc. XXVI Int. Conf. on High Energy Physics, Dallas, August 1992, J. Sanford editor (1993) 1101

    V. N. Gavrin et al., Nucl. Phys. B (Proc. Suppl.) 35 (1994) 412;

    J. N. Abdurashitov et al., Phys. Lett. B328 (1994) 234.

17. M. Spiro and D. Vignaud, Phys. Lett. 242B (1990) 279;

    V. Castellani , S. Degl'Innocenti and G. Fiorentini, Astron. Astrophys. 271 (1993) 601;

    N. Hata, S. Bludman and P. Langacker, Phys. Rev. D49 (1994) 3622.

18. N. Hata and P. Langacker, Phys. Rev. D52 (1995) 420.

19. S. Parke, Phys. Rev. Lett. 74 (1995) 839.

20. P. I. Krastev and S. T. Petcov, Phys. Rev. Lett. 72 (1994) 1960.

21. Review of Particle Properties, Phys. Rev. D50 (1994) 1315.

22. L. Wolfenstein, Phys. Rev. D17 (1978) 2369.

23. S. P. Mikheyev and A. Yu. Smirnov, Nuovo Cim. 9C (1986) 17.

24. N. Hata and P. Langacker, Phys. Rev. D50 (1994) 632.

25. K. S. Hirata et al., Phys. Rev. Lett. 66 (1991) 9.

26. T. Yanagida, Prog. Theor. Phys. B135 (1978) 66;

    M. Gell-Mann, P. Ramond and R. Slansky, in Supergravity, eds. P. van Nieuwenhuizen and D. Freedman (North Holland, Amsterdam 1979), 315.

27. S. Bludman, D. Kennedy and P. Langacker, Nucl. Phys. B374 (1992) 373; Phys. Rev. D45 (1992) 1810.

28. See the lectures by M. Spiro at this School.

29. M. de Jong et al., CERN-PPE/93-131 (1993).

30. NOMAD Collaboration, CERN-SPSLC/91-21 (1991);

    CERN-SPSLC/91-48 (1991); CERN-SPSLC/91-53 (1991); CERN-SPSLC/92-51 (1992);

    see also A. Rubbia, Nucl. Phys. B (Proc. Suppl.) 40 (1995) 93.

31. C. Albright and E. Schrock, Phys. Lett. B84 (1979) 123.

32. A. Astbury et al., Phys. Scripta 23 (1981) 397.

33. D. Autiero et al., The Electromagnetic Calorimeter of the NOMAD experiment (submitted to Nucl. Instrum. Methods).

34. K. Eggert et al., Nucl. Instrum. Methods 176 (1980) 217.

35. L. V. Volkova. Sov. J. Nucl. Phys. 31 (1980) 784;

    A. V. Butkevitch et al., Sov. J. Nucl. Phys. 50 (1988) 90;

    G. Barr, T. K. Gaisser and T. Stanev, Phys. Rev. D39 (1989) 3352;

    W. Frati et al., Phys. Rev. D48 (1993) 1140;

    D. H. Perkins, Nucl. Phys. B399 (1993) 3;

    H. Lee and Y. S. Koh, Nuovo Cim. B105 (1994) 883;

    B. C. Barish, Nucl. Phys. B (Proc. Suppl.) 38 (1995) 343.

36. K. S. Hirata et al., Phys. Lett. B205 (1988) 416;

    K. S. Hirata et al., Phys. Lett. B280 (1992) 146.

37. D. Casper et al., Phys. Rev. Lett. 66 (1991) 2561;

    R. Becker-Szendy et al., Nucl. Phys. B (Proc. Suppl.) 38 (1995) 331.

38. Ch. Berger et al., Phys. Lett. B227 (1989) 489;

    Ch. Berger et al., Phys. Lett. B245 (1990) 305;

39. M. Aglietta et al., Europhys. Lett. 8 (1989) 611.

40. M. C. Goodman, Nucl. Phys. B (Proc. Suppl.) 38 (1995) 337.

41.	Y. Fukuda et al., Phys. Lett. B335 (1994) 237.

42.	C. Athanassopoulos et al., Phys. Rev. Lett. 75 (1995) 2650.

43.	J. E. Hill, Phys. Rev. Lett. 75 (1995) 2654.

44.	B. Zeitnitz, Prog. Part. Nucl. Phys. 32 (1994) 351.

45.	B. Armbruster et al., Nucl. Phys. B (Proc. Suppl.) 38 (1995) 235.

46.	L. Borodovsky et al., Phys. Rev. Lett. 68 (1992) 274.

47.	J. Schneps, Nucl. Phys. B (Proc. Suppl.) 38 (1995) 220.

48.	E. Ables et al., Fermilab proposal P-875 (February 1995).

49.	A. Bettini et al., Nucl. Intr. Meth. A332 (1993) 395.

50.	H. H. Chen. Phys. Rev. Lett. 55 (1985) 1534.

51.	S. Bonetti, Nucl. Phys. B (Proc. Suppl.) 28A (1992) 486;

	M. Giammarchi, Nucl. Phys. B (Proc. Suppl.) 35 (1994) 433.

52.	P. Vogel, Nucl. Phys. B (Proc. Suppl.) 38 (1995) 204.

53.	M. Koshiba, Phys. Rep. 220 (1992) 358.